Accepted to Phys. Fluids 10.1063/5.0165467

Modeling and Simulation of Flow-Osteocyte Interaction in a Lacuno-canalicular network

Jared Barber, Isaac Manring, Sophie Boileau, and Luoding Zhu (祝罗丁)*

Department of Mathematical Sciences, Indiana University Purdue University Indianapolis, 402 N Blackford Street, LD 270, Indianapolis, IN 46202, USA

jarobarb@iupui.edu, imanring@iupui.edu, boileaus@carleton.edu, luozhu@iupui.edu

* The author to whom correspondence may be addressed: luozhu@iupui.edu

Abstract

Osteocytes are bone cells that can sense mechanical cues (stress and strain) and respond by releasing biochemical signals that direct bone remodeling. This process is called mechanotransduction which, in osteocytes, is not well understood yet because *in vivo* studies have proven difficult due to the complexity and inaccessibility of the flow-osteocyte-lacuna-canaliculi (FOLC) system. While *in silico* studies (modeling and simulation) have become powerful, currently computational studies for the system often omit the fluid-structure-interaction (FSI) between the cell and the surrounding fluids. To investigate the role of FSI in osteocyte mechanotransduction, we introduce a two-dimensional coarse-grained yet integrative model for flow-osteocyte-interaction in a lacuno-canalicular network. The model uses the lattice Boltzmann immersed boundary (LB-IB) framework to incorporate the flexible osteocyte (membrane, cytoskeleton and cytosol), its processes, the interstitial fluid, and the rigid extracellular matrix that encases the system. One major result of our model is that the stress and strain tend to attain their local maxima near the regions where the processes meet the membrane of the main body.

Key words: *interstitial flow, viscous incompressible flow, osteocyte, lacuno-canalicular network, mechanotransduction, lattice Boltzmann equations, immersed boundary method, modeling and simulation*

1. Introduction

It is known that osteocytes (the most common type of bone cell) are responsible for converting mechanical cues to biochemical signals whose presence or absence can lead to growth or degradation of bone tissue. This process called mechanotransduction (MT) is not yet well understood, especially at the cellular level. For example, it is not certain which part of the osteocyte actually perceives the mechanical forces and deformation [1, 2]. An osteocyte is surrounded by osteocyte-associated proteins known as the pericellular matrix (PCM) and by interstitial viscous fluid, all of which is embedded inside a complicated lacuno-canalicular network. The network surrounding an osteocyte

This is the author's manuscript of the article published in final edited form as:

Barber, J., Manring, I., Boileau, S., & Zhu, L. (祝罗丁). (2023). Modeling and simulation of flow–osteocyte interaction in a lacuno-canalicular network. Physics of Fluids, 35(9), 091910. https://doi.org/10.1063/5.0165467

consists of an ellipsoidal hole (i.e. a lacuna, housing the cells' main body) and 60+ curved and tapered tunnels (i.e., canaliculi, each housing a process and connecting to other osteocyte regions). The lacuna and canaliculi have complicated geometries that include irregular or rough wall surfaces and are all encased in hard bone matrix (extracellular matrix or ECM). Because of the complexity of the fluid-osteocyte-lacuna-canaliculi system and its inaccessibility due to the surrounding calcified bone matrix, *in vivo* studies of the system prove to be difficult. Rather, *in-silico* studies are appropriate and have been frequently used to gain insight into this system. However, many such computational studies are limited because they considered only one or a select few components, which can cause them to miss potentially important inter-component interactions. Additionally, such studies seldom considered the potential effects of fluid-osteocyte interaction.

Weinbaum *et al.* [3] and Klein-Nulend *et al.* [4] studied the interstitial fluid flow past an osteocyte process and through pericellular matrix (PCM) in a detached canaliculus. You *et al.* [5], Han *et al.* [6], and Wang *et al.* [7] proposed isolated process models with ultrastructure that included tethering elements that connected the process membrane to the canalicular wall. The interstitial flow was modelled as a prescribed drag on the tethering elements. Anderson *et al.* [8] and Kamioka *et al.* [9] investigated the effects of canalicular wall roughness on the flow and shear stress in a single isolated canaliculus. Verbruggen *et al.* [10] used experimental images and modeled the osteocyte, PCM, and ECM as elastic solids (no fluids) to show that physiologically realistic geometries and the presence of PCM can enhance strain amplification. Wang *et al.* [11] investigated strain amplification of the osteocyte-lacuna-canaliculi system during cyclic loading using a finite element solid model (no flow) and found that strain amplification depended on the frequency and amplitude of the loading. Schurman *et al.* [12] used the commercial software COMSOL to create an image-based osteocyte model with 20+ curved canaliculi without processes. They found that the canalicular tortuosity did not have a significant effect on flow shear stress. All of these works considered only parts of the entire osteocyte-fluid-lacuna-canaliculi system and did not consider fluid-structure-interaction.

Verbruggen *et al.* [13] considered fluid-structure interaction by building 4 image-based and one idealized model for osteocytes in a lacuno-canalicular system. In all these models, the osteocyte and its processes were modelled as linearly elastic homogeneous solids (including the cytoplasm) using finite element methods. Static loading was applied on one side of the cubic ECM-interstitial fluid-osteocyte domain. Commercial software ANSYS was used for computation. Their simulations found that the greatest mechanical stimulation occurred in the processes and was enhanced by canalicular wall roughness. Vaughan *et al.* [14] similarly modeled the osteocyte model as a homogeneous solid and used ANSYS to study the role of integrin attachment and primary cilium. Verbruggen *et al.* [15] used an idealized symmetric and elastically homogeneous osteocyte model and ANSYS to computationally investigate the effects of canalicular curvature. Their results suggested that increased canalicular tortuosity led to increased strain stimulation. Joukar *et al.* [16] modeled an osteocyte with 10 processes and their canaliculi by using linearly elastic isotropic finite elements and ANSYS. They found that canaliculi orientation compared to the loading direction could affect the fluid velocity, shear stress, and mechanotransduction signal in the system. Kameo *et al.* [17] combined the finite element, immersed boundary, and lattice Boltzmann methods to consider interstitial flow past a single process in a canaliculus. They found that decreased PCM density and increased canaliculus curvature enhance local strain. Ganesh *et al.* [18] discussed how finite element modeling and simulation of mechanical loading can be used to investigate interstitial flow, stress, and strain of an osteocyte in the lacuno-canalicular system and shared their FSI work involving an idealized osteocyte with 18 straight canaliculi.

As a first attempt to consider mutual interactions among the fluid extracellular (interstitial) and intracellular, osteocyte main body, and cellular processes, the goal of this paper is to build a coarse-grained, minimal yet integrative, mathematical model in two dimensions to investigate the possible synergistic effects of the system's various components (both fluid and solid).

The osteocyte membrane, cytoskeleton, and its processes are modelled by elastic fibers with different elasticities. The extracellular (interstitial) and intracellular flows are modelled by the lattice Boltzmann equations. The flow-osteocyte interaction is modelled by the immersed boundary framework. The major differences between our model and the other FSI models mentioned above are as follows. First, in the existing works, the osteocyte and process are frequently modeled as linearly elastic homogeneous solids that have no fluid component; in our work the osteocyte membrane, cytoskeleton, and process can have different elasticities and the osteocyte has both solid and fluid components (i.e. biphasic). Secondly, the mechanical loading is usually static in existing works while it is both static and cyclic here.

This model builds, to some extent, on a past model produced by the authors [28]. Both works used the two-dimensional lattice Boltzmann method to model flow in a lacuno-canalicular cavity, including very similar boundary condition implementations. The previous work, however, used a rigid osteocyte model without any processes or fluid-structure interaction. It also included up to 64 randomly constructed canaliculi and pericellular matrix (modelled as rigid particles) in the lacuna and the canaliculi. It found that pericellular matrix could enhance stress near the cell and that the number and geometry of canaliculi have some quantitative but not qualitative influence on the shear stress on the osteocyte body. The current work introduces a flexible cell with multiple components while sacrificing canaliculi complexity and pericellular matrix inclusion to maintain a tractable study. This allows us to pursue our goal of introducing a minimal integrative FSI model to investigate the possible effects of fluid-structure-interaction and synergistic interactions among various osteocyte components.

Although our model is coarse grained and two-dimensional, it is integrative and incorporates FSI: namely it includes each major component of the FOLC system – the osteocyte membrane, cytoskeleton, cytosol, cellular process, interstitial fluid, and the mutual interactions among these elements. The model is based on the lattice-Boltzmann immersed boundary framework [19-21]. One of our findings is that the stress and strain tend to attain their local maxima near the regions where the processes meet the membrane of the osteocyte's main body. This encourages increased attention in studies to such junctions for the reasons given below.

Mechanotransduction starts with mechanosensation and higher stresses and strains are more likely to exceed mechanosensation thresholds and initiate mechanoresponses. In fact, a well-known issue with osteocyte mechanotransduction is that the stresses/strains necessary to initiate significant osteocyte responses in vitro are 10x higher than the average macroscale forces bones experience during everyday activities like walking and running. Osteocytes need high stresses to undergo mechanotransduction. One possible way to achieve higher stresses while still being subjected to a low average stress is for stresses to be highly concentrated or localized at a select few locations. This possibility has been explored by others including proposals that tethers attaching osteocytes to lacuno-canalicular walls may provide the needed concentration of stress [7]. High localized stresses causing osteocyte mechanotransduction is a hypothesis actively being explored by modelers and experimentalists alike. Our contribution, we hope, will inspire new laboratory experiments that look for mechanosensors near the osteocyte main body-process junctions.

The remaining of the paper is as follows. Section 2 describes the FOLC model. Section 3 outlines the mathematics of the model. Section 4 addresses the numerical methods for solving the mathematical equations. Section 5 reports and discusses the major computational results. Section 6 concludes the paper with a summary and further discussion.

2. Coarse-grained model of the fluid-osteocyte-lacuna-canaliculi (FOLC) system

The model is depicted in Fig. 1. The osteocyte's main body is modelled as a deformable ellipse enclosing a viscous incompressible fluid (cytoplasm). Its cytoskeleton is coarse-grained as 8 elastic fibers or links. The fibers are symmetrically distributed and each attaches the osteocyte center to the elliptical membrane. The processes are coarse-grained as 4 sinusoidal elastic fibers symmetrically distributed along the northern, western, southern, and eastern directions. The fibers resist both stretching/compression and bending. Each fiber is attached to the osteocyte membrane at one end and is either allowed to freely move (western and eastern; usually next to outlet boundaries) or fixed in space by an anchored ghost point (northern and southern; usually next to inlet boundaries) at the other end. The lacuna is modelled as an elliptic cavity concentric to the osteocyte and each canaliculus is modelled as a sinusoidal opening centered about the process. The interstitial fluid in the gap between the cell membrane (osteocyte main body and processes) and the lacuno-canalicular wall is modelled as water. The extracellular matrix (ECM) encasing the fluid-osteocyte-lacuna-canaliculi (FOLC) system is modelled as rigid material. We note that each component of the osteocyte (membrane, cytoskeleton, and processes) may have different elasticities and all of them are immersed in and interact with the ambient fluid in our FOLC model.

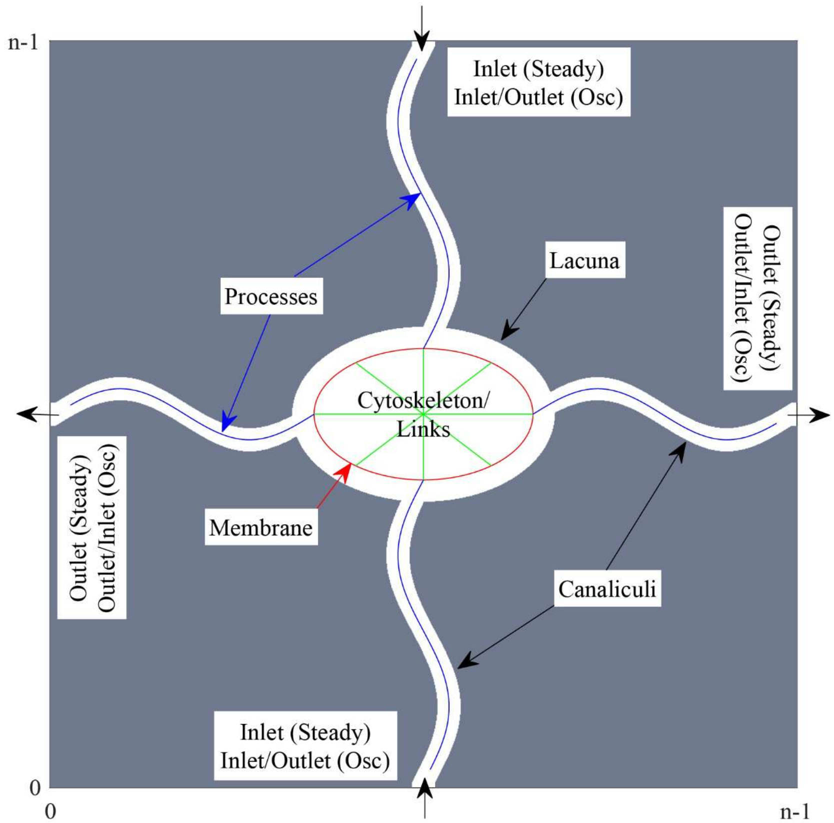

Fig. 1 Illustration of the FOLC Model. The computational domain consists of a solid region (gray), fluid region (white), and fibers immersed in the fluid including fibers representing the cell's membrane/cortex (red), its cytoskeleton (green), and its processes (blue). All simulations use $n = 1024$ unless stated otherwise.

To justify the above coarse-grained approach for processes, we note that each osteocyte has many curved and tapered dendritic structures called cellular processes. Each process consists of a process membrane, cytosol, and a bundle of actin filaments oriented longitudinally down the center of the process. The actin filaments in the bundle are cross-linked by fibrin and the bundle is attached to the process membrane by cross filaments. The average process diameter is 104 ± 69 nm while its length is approximately 20 μm [22, 23]. In contrast, the main body of the osteocyte resembles an almond whose depth is approximately 7 μm and is 5 to 20 microns across the flatter directions [24]. Compared to the osteocyte's main body, the processes are very slender so that modeling it as an elastic fiber provides a good first approximation to the process's structure. For more details please see the paper on the ultrastructure of processes [22].

A cartesian orthogonal rectangular coordinate system is used with the origin set at the southwestern corner. A computational domain (-0.5,1023.5)×(-0.5,1023.5) in lattice Boltzmann (LB) units is discretized as a family of grid points with x-coordinates (0,1,2,…,1023) and y-coordinates (0,1,2,…,1023). In Fig. 1, black pixels represent the rigid ECM and white ones represent the extracellular (interstitial) and intracellular (cytosol) fluids. Flexible curves represent the osteocyte's main body including the cytoskeleton (8 fibers; green) and an elliptical membrane (red). The osteocyte is centered at (511.5,511.5) with semi-major and semi-minor axis lengths of 150 and 90. The gap between the osteocyte membrane (inner red ellipse) and the ECM wall (outer black elliptical region) is 30 LB units thick. The curved channels modeling the canaliculi are 32 units wide and each contains a cellular process/dendrite (blue). The fixed end of the dendrite on the north and south is 25.0 LB units away from the canalicular outer edge. During steady flow, the fluid flows in from the north and south canaliculi and flows out via the west and east ones. The computational domain was generated by first creating the solid components including the membrane (ellipse) and processes (sine curves) and then making all points outside the ellipse and within 30 or 32/2 units of the solid components, as appropriate, in the 1024×1024 lattice into fluid nodes while the other nodes were set to be solid. Additionally, to simplify boundary condition implementation, the inlets and outlets were made to be straight for the last 8 nodes as they headed towards the outer boundary. All length quantities were divided by 2 and 4 for the 512×512 and 256×256 grids, respectively, which were used in our convergence study.

We consider only one set of inlets/outlets for the static and oscillatory cases. In reality, all of the osteocytes are connected to each other via the numerous processes in the canaliculi, and there is no inlet or outlet since flow entering the region near the osteocyte through a canaliculus at one moment may switch directions at the next moment and vice versa when the person is in motion. Due to this complexity, scientists frequently model the osteocyte region using only one or at most a handful of inlet/outlet/boundary condition arrangements [15, 16, 18, 25]. Also, in most models above, constant pressure at inlets is used. In our work, it is more convenient to use prescribed velocity at inlets as it is relatively easy to define those velocities given the Reynolds number being considered in the lattice Boltzmann method.

We use both static and oscillatory boundary conditions. This choice approximates biological reality to simplify computations. In reality, interstitial fluid flows in and out of canaliculi as a person walks or runs. We assume/consider only regular motion where flow becomes oscillatory with constant period. This simplifying assumption ignores irregular motion where the flow in the canaliculi may be much more complex. To consider both the frequently modeled steady flow and less modeled but more physiologically realistic oscillatory flow, we use both uniform and oscillatory flow boundary conditions at the inlets and outlets. In addition, the steady state represents extreme behavior in the system corresponding to oscillations that take place over much longer time periods. This gives us an additional case to use when considering how oscillations, especially their frequency, may affect dynamics.

3. Mathematical formulation of the FOLC model

The above FOLC system is modeled using a nonlinear system of differential and integral equations. The extracellular (interstitial) and intracellular (cytosol) fluids are assumed to be viscous,

Accepted to Phys. Fluids 10.1063/5.0165467

incompressible, and Newtonian with the mechanical properties (mass density and dynamic viscosity) of water. The fluid flows are governed by the classic Navier-Stokes equations:

$$\rho\frac{\mathrm{D}\mathbf{u}}{\mathrm{D}t} = -\boldsymbol{\nabla} p + \mu\Delta\mathbf{u} + \mathbf{f}; \qquad (1)$$
$$\boldsymbol{\nabla}\cdot\mathbf{u} = 0. \qquad (2)$$

Here $\mathbf{u}$, p, ρ, t, and μ are the fluid velocity, pressure, mass density, time, and fluid dynamic viscosity, respectively. The symbol $\frac{\mathrm{D}}{\mathrm{D}t}$ in Eq. 1 is the material derivative (total derivative), i.e., $\frac{\mathrm{D}}{\mathrm{D}t} = \frac{\partial}{\partial t} + \mathbf{u}\cdot\boldsymbol{\nabla}$. Here $\mathbf{f}$ represents the Eulerian force density (defined on the fluid) applied by the osteocyte (i.e. its constitutive fibers for the membrane, cytoskeleton, and processes) to the fluid. It is computed from its Lagrangian equivalent $\mathbf{F}$ (defined on osteocyte) as follows:

$$\mathbf{F}(\alpha,t) = -\frac{\partial(\mathcal{E}_s+\mathcal{E}_b)}{\partial\mathbf{X}}, \quad \mathcal{E}_s = \frac{K_s}{2}\int\left(\left|\frac{\partial\mathbf{X}}{\partial\alpha}\right| - 1\right)^2 d\alpha, \quad \mathcal{E}_b = \frac{K_b}{2}\int(\kappa-\kappa_0)^2 d\alpha, \quad (3-5)$$

$$\kappa = \left(\frac{\frac{\partial\boldsymbol{X}}{\partial\alpha}\times\frac{\partial^2\boldsymbol{X}}{\partial\alpha^2}}{\left|\frac{\partial\boldsymbol{X}}{\partial\alpha}\right|^3}\right)\cdot\hat{\boldsymbol{z}} \qquad (6)$$

Here κ and κ_0 are the signed curvature and reference curvature. Note that we have relaxed the small deformation assumption for the solid motion and also allowed fibers to have non-zero reference curvature. We use the initial curvature as the reference curvature so that all components are initially stress-free and the links, which start straight, have zero reference curvature while processes and membrane components have nonzero initial/reference curvature (Fig. 1). In Eqs. 3-5 above, the elastic potential energy density ($\mathcal{E} = \mathcal{E}_s + \mathcal{E}_b$) may have contributions from stretching/compression ($\mathcal{E}_s$) and from bending ($\mathcal{E}_b$) of the fibers. K_s and K_b are the stretching/compression coefficient and bending rigidity, respectively. These coefficients are constant for each component (membrane, process, cytoskeleton/links) but are sometimes varied across components so that, for example, the processes may be more rigid than the membrane or vice versa.

The vector $\mathbf{X}(\alpha,t)$ denotes the Eulerian coordinates of a Lagrangian point labeled by α at time instant t. The variable α is the Lagrangian coordinate of a typical point on a constitutive fiber. To mediate the fluid-osteocyte interactions, we use the immersed boundary method. In the method, the Lagrangian force exerted by the fibers on the fluid ($\mathbf{F}(\alpha,t)$) is transferred to an Eulerian fluid body force ($\mathbf{f}(\mathbf{x},t)$). The Navier-Stokes equations with that body force are numerically solved for the fluid velocity ($\mathbf{u}(\mathbf{x},t)$) and pressure ($p(\mathbf{x},t)$). The osteocyte's velocities, $\mathbf{U}(\alpha,t)$, and subsequent motion is obtained by interpolating the fluid velocities onto the osteocyte's nodes. The equations for the force transfer and velocity interpolation steps use the two integrals:

$$\mathbf{f}(\mathbf{x},t) = \int\mathbf{F}(\alpha,t)\delta\big(\mathbf{x}-\mathbf{X}(\alpha,t)\big)d\alpha, \qquad \mathbf{U}(\alpha,t) = \int\mathbf{u}(\mathbf{x},t)\delta\big(\mathbf{x}-\mathbf{X}(\alpha,t)\big)d\mathbf{x}. \qquad (7-8)$$

Here $\delta(\mathbf{x})$ is the classic Dirac delta function. Note that these two equations, as of yet, contain no approximations and coupling them with Eqs. 1-6 will result in the exact, not approximate, dynamics of the solid components. See Peskin [26] for details.

The fluid's initial velocity is set to zero and the mass density to that of water across the whole lacuno-canalicular space. A no-slip boundary condition is used on the lacuno-canalicular wall. Fluid velocity is imposed at the north and south canalicular boundaries. Free boundary conditions are applied at the west and east canalicular boundaries. Initially the osteocyte membrane is in the shape of an ellipse centered in the lacuna, the cellular processes are initially positioned in the middle of the canaliculi in the shape of a sine wave, and the links are straight line segments emanating from the center of the osteocyte towards the membrane.

3. Numerical methods

Lattice Boltzmann Method

The Navier-Stokes equations are numerically solved by the lattice Boltzmann method (the D2Q9 model) [27-32]. In our lattice Boltzmann method, at each lattice location in the rectilinear grid with unit spacing, distribution functions g_j track the amount of particles traveling in each of nine directions ($\boldsymbol{\xi}_0 = (0,0)$, $\boldsymbol{\xi}_1 = (1,0)$, $\boldsymbol{\xi}_2 = (0,1)$, $\boldsymbol{\xi}_3 = (-1,0)$, $\boldsymbol{\xi}_4 = (0,-1)$, $\boldsymbol{\xi}_5 = (1,1)$, $\boldsymbol{\xi}_6 = (-1,1)$, $\boldsymbol{\xi}_7 = (-1,-1)$, $\boldsymbol{\xi}_8 = (1,-1)$). The particles at that location are allowed to collide with each other, which results in altered distributions after the collision step given by:

$$\tilde{g}_j(\mathbf{x},t) = g_j(\mathbf{x},t) - \frac{1}{\tau}\left(g_j(\mathbf{x},t) - g_j^0(\mathbf{x},t)\right) + \left(1 - \frac{1}{2\tau}\right) w_j \left(\frac{\boldsymbol{\xi}_j - \boldsymbol{u}(\boldsymbol{x},t)}{{c_s}^2} + \frac{\boldsymbol{\xi}_j \cdot \boldsymbol{u}(\boldsymbol{x},t)}{{c_s}^4}\boldsymbol{\xi}_j\right) \cdot \mathbf{f}(\mathbf{x},t) \quad (9)$$

$$g_j^0(\mathbf{x},t) = w_j \rho \left(1 + \frac{\boldsymbol{\xi}_j \cdot \mathbf{u}}{c_s^2} + \frac{\left(\boldsymbol{\xi}_j \cdot \mathbf{u}\right)^2}{2c_s^4} - \frac{\mathbf{u}\cdot\mathbf{u}}{2c_s^2}\right). \quad (10)$$

Here τ is the particle relaxation time, $c_s = 1/\sqrt{3}$ is the lattice speed of sound, and $w_j = 4/9$ for $j = 0$; $w_j = 1/9$ for $j = 1,2,3,4$; and $w_j = 1/36$ for $j = 5,6,7,8$. In addition, particles are allowed to stream from one lattice location to another, called a streaming step and given by:

$$g_j\left(\mathbf{x} + \boldsymbol{\xi}_j, t+1\right) = \tilde{g}_j(\mathbf{x},t) \quad (11)$$

Repeating these steps we can then use

$$\rho = \sum_{j=0}^{8} g_j \text{ and } \rho\mathbf{u} = \sum_{j=0}^{8} g_j\, \boldsymbol{\xi}_j + 0.5\mathbf{f}(\mathbf{x},t) \quad (12-13)$$

to obtain approximate solutions for the densities and velocities that solve Navier-Stokes equations.
In addition, appropriate combinations of distribution functions can be used to yield estimates for the stress in the fluid at any location on the lattice/the fluid grid:

$$\boldsymbol{\sigma} = -\left(1 - \frac{1}{2\tau}\right)\sum_{i=0}^{8} g_j^{neq} \boldsymbol{\xi}_i \otimes \boldsymbol{\xi}_i - \frac{1}{2}\left(1 - \frac{1}{2\tau}\right)(\mathbf{f}\otimes\mathbf{u} + \mathbf{u}\otimes\mathbf{f}). \quad (14)$$

Here, $g_j^{neq} = g_j - g_j^0$ and $\mathbf{f}$ is the force density from earlier.

Boundary conditions

For no-slip boundary conditions, the half-way bounce-back scheme is applied on the lacuno-canalicular wall. During the streaming step, the scheme reflects distributions hitting a wall back in the direction they came from: $g_{\bar{j}}(\mathbf{x}, t+1) = \tilde{g}_j(\mathbf{x},t)$ where $\bar{j}$ corresponds to the distribution function for particles headed in the opposite direction of the particles corresponding to the j^{th} direction.

The velocity profile used at the north and south inlets for steady flow were set to a constant incoming velocity, as determined by the Reynolds number. At the outlet, we allow free outflow using our 3D Zou-He boundary condition applied with extrapolated momenta. For oscillatory flow, the north and south velocity profile is still a prescribed velocity that is constant with respect to space but now varies in time: $\mathbf{u}_{\text{in}} = \mathbf{u}_{\text{char}} \sin(2\pi f_o t)$ where f_o is the oscillation frequency. At the east and west canaliculi, the same 3D Zou-He boundary condition with extrapolated momenta is applied.

For implementing the inlet and outlet boundary conditions, we follow [32] and use Zou-He or non-equilibrium bounce-back schemes. At any inlet or outlet lattice location, streaming naturally gives estimates for six of the nine distribution functions at the next time step while three of the distribution functions, which can be thought of as streaming in from outside the computational domain, are unknown. In addition, if the velocities or momenta at the boundary are known, the density at that location is the only other unknown. To find these four unknowns, we use four equations, the density and momenta Eqs. 12-13 and the demand that the non-equilibrium distribution perpendicular to the boundary is bounced back: $g_{\bar{j}}(\mathbf{x}, t+1) - g_{\bar{j}}^0(\mathbf{x}, t+1) = \tilde{g}_j(\mathbf{x}, t) - \tilde{g}_j^0(\mathbf{x}, t)$ (non-equilibrium bounce-back; [33]). At the north and south boundaries, the incoming velocities are prescribed and the four unknowns are solved for. At the east and west boundary to solve for the four unknowns, we use "prescribed" horizontal and vertical momenta by extrapolating momenta from the interior to the boundary: e.g., at the left side, $\rho_{i_{left},j}\mathbf{u}_{i_{left},j} = \rho_{i_{left}+1,j}\mathbf{u}_{i_{left}+1,j} + K(m_{curr} - m_{des})\mathbf{n}$. The final term on the right, which includes the outward normal $\mathbf{n}$ at the boundary, is a correction term that adjusts the outgoing flux to ensure that our current total mass (m_{curr}) stays close to our initial or desired total mass (m_{des}) in the system. Using $K = 1$ makes it so that $(m_{curr} - m_{des})/m_{des} = \pm\mathcal{O}(1 \times 10^{-10})$.

Solid force discretization and calculation

To discretize Eqs. 3-5, the Lagrangian coordinates on a fiber (e.g. the membrane, a link, or a process) are discretized into n initially equidistant points (α_j; $\Delta\alpha$ units apart). Derivatives with respect to the Lagrangian coordinate α are then approximated using centered differences and the corresponding integrals approximated using the midpoint (Eq. 4) or trapezoidal rule (Eq. 5):

$$\mathcal{E}_s \approx \frac{K_s}{2}\sum_{j=1}^{n-1}\left(\left|\frac{\mathbf{X}_{j+1} - \mathbf{X}_j}{d\alpha}\right| - 1\right)^2 \Delta\alpha; \quad \mathcal{E}_b = \frac{K_b}{2}\sum_{j=1}^{n-1}\left(\kappa_j - \kappa_{j,0}\right)^2 \Delta\alpha. \quad (14-15)$$

Here $\mathbf{X}_j$ is the Eulerian location of the piece of material associated with Lagrangian coordinate α_j. The curvature (and reference/initial curvature) is estimated using:

$$\kappa_i \approx 8\frac{(\mathbf{X}_i - \mathbf{X}_{i-1}) \times (\mathbf{X}_{i+1} - \mathbf{X}_i)}{\|\mathbf{X}_{i+1} - \mathbf{X}_{i-1}\|^3} \cdot \hat{\mathbf{z}}. \qquad (16)$$

Where $\hat{\mathbf{z}}$ is a unit vector normal to the x-y plane. The variational derivative in Eq. 3 is then approximated by taking the variational derivatives of the discretized energies with respect to each discretized node on the fiber. Many assume small deformation and consider the case of zero reference curvature, which allows one to approximate the curvature using $\left|\frac{\partial^2\mathbf{X}}{\partial\alpha^2}\right|$ in Equation 5 (assume small deformation i.e. that $\frac{\partial\mathbf{X}}{\partial\alpha}$ is nearly a tangent unit vector and compare with Eq. 6). While this greatly simplifies the variational derivative, our simulations suggested that using the curvature as written in Eq. 6 (discretized in Eq. 16) without any small deformation assumptions produces significantly more stable simulations. Because the variational derivative in that case is significantly more complicated, we have placed details for this nontrivial case in the appendix.

Fluid-structure interaction

To obtain the force due to the solid components at fluid grid locations, Eq. 7 for the spreading operator must be discretized. This is accomplished by evaluating the line integral using the trapezoidal rule and replacing the Dirac delta function with a discretized/approximate version of the function. Here, the Dirac delta function is discretized by functions frequently used in the IB method [26]:

$$\delta_{2D} = \frac{1}{h^2}\delta_{1D}(x)\delta_{1D}(y); \ \delta_{1D}(r) = \begin{cases} (3 - 2|r| + \sqrt{1 + 4|r| - 4r^2})/8 & |r| < 1 \\ (5 - 2|r| - \sqrt{-7 + 12|r| - 4r^2})/8 & 1 \le |r| < 2 \\ 0 & 2 < |r| \end{cases} \quad (17)$$

Here $r = \frac{x}{h}$ or $r = \frac{y}{h}$ and $h = 1$ is the mesh spacing. In a similar fashion, the interpolation is accomplished by applying a two-dimensional midpoint rule to the integral over the area of the domain. The same discrete delta function with an appropriately adjusted argument is used.

Local stress estimation

During the immersed boundary algorithm, forces in the solids are calculated (see "Solid force discretization and calculation"). In theory, summation of these forces should be equal and opposite to the forces in the fluid so that one can use such solid forces to estimate the fluid forces acting on the solid components, which is of primary interest when considering potential externally initiated mechanosensation. However, for low enough Reynolds numbers/high enough elastic moduli and longer time scales, numerical effects can cause force estimates to become oscillatory with respect to distance along a solid fiber. The immersed boundary method's spreading and interpolation operations effectively smooth out such oscillations so that the overall cell motion is still realistic, non-oscillatory, and convergent (Fig. 2). Nonetheless, due to our interest in the local forces, we implemented two smoothing procedures to provide more accurate estimates for visualizing the local fluid stresses acting on the cell.

The first smoothing procedure was used to obtain more accurate estimates of the stresses and stress-related quantities at all locations along the solid components at a select few times. In that procedure, we used a radial basis function approach combined with local quadratic least squares fits akin to a modified Shepard algorithm (e.g. [34]) to extrapolate stress tensor components (Eq. 14) and pressure to the solid grid (see Appendix B). The second smoothing procedure was used to obtain estimates for the average stresses along each type of component (membrane, processes, links) over multiple times. In the second smoothing procedure, we used diffusion-based smoothing on each fiber before averaging across all fibers for each type of component. In particular, along a given fiber the local solid force was averaged $n_{smooth} = 10$ times using the procedure $\mathbf{F}_{i,new} = (\mathbf{F}_{i,curr} + (\mathbf{F}_{i-1,curr} + \mathbf{F}_{i+1,curr})/2)/2$. Along the ellipse, periodic averaging/wraparound was performed at the fiber's "ends". Along the other fibers, one-sided averaging of the form $\mathbf{F}_{i,new} = (\mathbf{F}_{i,curr} + (\mathbf{F}_{i,curr} + \mathbf{F}_{i+1,curr})/2)/2$ was performed. Given the number of discretized points on each fiber varies from 257 to 1401, how we handled the endpoints had relatively little effect on our results. After the smoothing procedure, the force magnitudes were then averaged using an arithmetic mean (Figs. 11 and 12).

4. Verification and validation

The immersed boundary (IB) and lattice Boltzmann (LB) methods have each been well tested and validated separately for a variety of applications. See [26, 30, 35] and references therein. The verification and validation of the lattice-Boltzmann based immersed boundary method (LB-IB) has been addressed in previous works [19, 20, 36, 37] in three dimensions. To make sure the implementation of the methods in two dimensions for our FOLC problem is correct, we performed convergence tests using successively refined grids of size $n =$ 256, 512, 1024, and 2048 shown in Fig. 2. Changing the grids also required appropriate rescaling of elastic moduli and time scales while the Reynolds number was held constant. The results in Fig. 2(a-b) show that as the grid is refined, the speed distributions are approximately the same when compared with each other (at the same rescaled times). Similarly, after appropriate recentering and rescaling of the dimensions of the system ($\tilde{x} = (x - x_0)/n$, $\tilde{y} = (y - y_0)/n$ with $x_0 = y_0 = (n-1)/2$), Fig. 2(c-d) show convergence of the cell deformations towards a unique solution (256×256-green; 512×512-red; 1024×1024-blue;

2048x2048-black). To balance accuracy and efficiency, we use the 1024×1024 grid for the rest of this study.

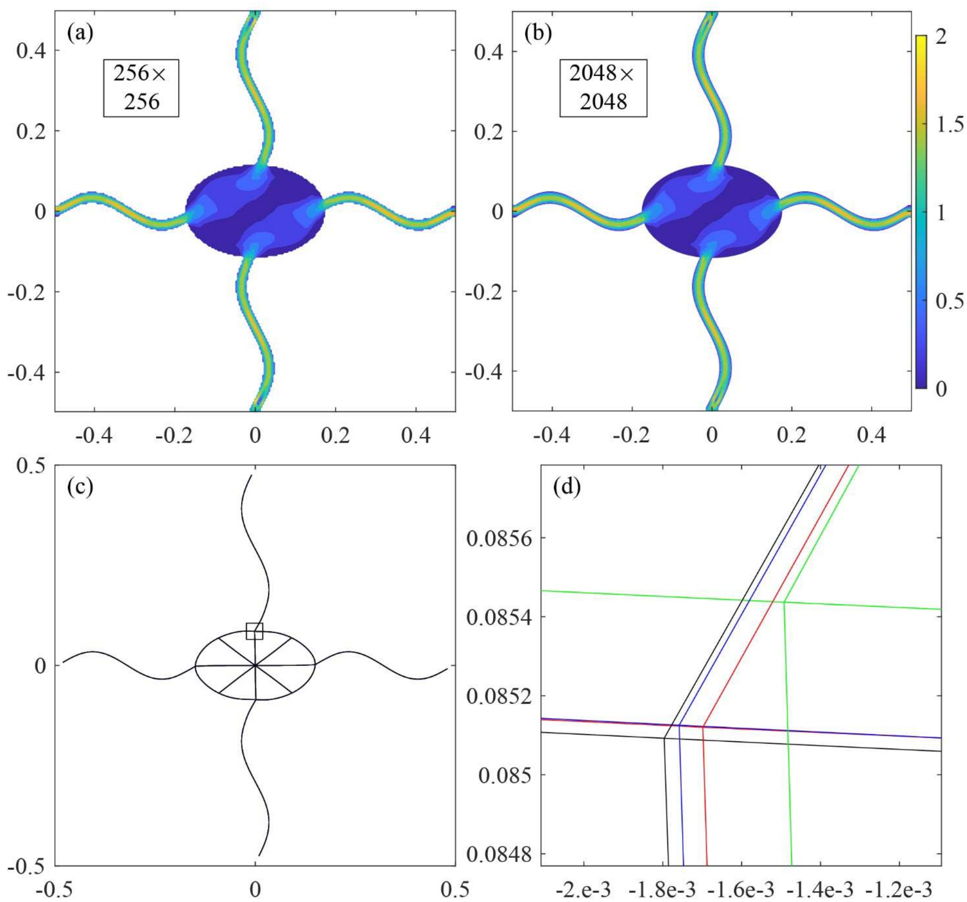

Fig. 2: Convergence study. Dimensional analysis shows that 6.25k time steps on a 256×256 grid is equivalent to 25k time steps on a 512×512 grid, to 100k time steps on a 1024×1024 grid, and to 400k time steps on a 2048×2048 grid. Plots are shown for simulations at those times using appropriately scaled elastic moduli (for 1024×1024, $(K_s, K_b) =$ (1.2 dyn/cm, 9e-10 dyn-cm)). (a-b) show nearly equivalent normalized speeds (speed divided by the inlet speed) that are difficult to differentiate by eye. Similarly, comparisons of the amount of deformation of the cell (256×256-green; 512×512-red; 1024×1024-blue; 2048×2048-black) are nearly indistinguishable after renormalization of the x and y coordinates ($\tilde{x} = (x - x_0)/n$, $\tilde{y} = (y - y_0)/n$ with $x_0 = y_0 = (n-1)/2$) in (c). Differences only become apparent after zooming in. (d) Near the membrane-link-process junction (box in (c)) we see convergence as refinement is increased. Other locations show similar trends.

To quantify convergence, we compared fluid velocities and pressure and solid positions for successively refined grids. For a general method with order accuracy p, we expect that for successively refined meshes using n^2, $(2n)^2$, $(4n)^2$, etc. points, successive differences obey $\|\mathbf{s}_a(2n) - \mathbf{s}_a(4n)\| \approx \|\mathbf{s}_a(n) - \mathbf{s}_a(2n)\|/2^p$. $\mathbf{s}_a(n)$ is the approximate solution on the $n \times n$ grid. The relationship can also be used to estimate p. See Appendix C for more details.

		$\|\mathbf{s}_a(n) - \mathbf{s}_a(2n)\|$			p estimates	
		256 v. 512	512 v. 1024	1024 v. 2048	256, 512, 1024	512, 1024, 2048
Fluids	u	0.0607	0.0263	0.0113	1.21	1.22
	v	0.0691	0.0315	0.0113	1.23	1.48
	p	0.025	0.019	0.0078	0.39	1.28
Solids	x	3.69e-4	1.05e-4	3.05e-5	1.81	1.78

Tab. 1: Average differences between fluid velocities, pressure, and solid node positions (see text for more details). The table suggests that errors improve with successive refinement as differences between successive solutions get smaller and smaller. Additionally, results suggest convergence of order $1 \leq p \leq 2$ in l_1 norm, which is in line with theory [30, 38].

Table 1 shows the successive differences and illustrates a clear trend towards smaller and smaller errors. In addition, the average nondimensionalized fractional differences for the fluid velocities indicate errors of around 6-7% decaying down to 1%. The pressure errors are even lower but caution must be used as the pressure is estimated using the lattice Boltzmann density, which serves a dual role with its magnitude corresponding to the actual mass density of the fluid and its variations corresponding to pressure fluctuations. The errors on the solids are likewise relatively small with deviations on the order of 10^{-4} on a unit square domain. The estimated values for the order of accuracy p's are between $1 \leq p \leq 2$, in line with typical values for lattice Boltzmann ($p = 2$, [39]) and immersed boundary ($p = 1$, [38]) theory. There is a p-value of 0.39 for pressure, but it is still a positive value and its low value is likely due to a combination of use of coarser meshes and the dual role of the lattice Boltzmann's ρ.

5. Major results

In this section, the main computational results will be presented in the following order. First, we consider the motion of the fluid and deformation of the osteocyte (membrane, cytoskeleton, and processes). Then we consider the fluid shear and normal stresses on the osteocyte membrane and processes. Finally, we consider the strains within the osteocyte. In each of these subsections, both static and cyclic loadings will be reported to show how results can contrast when oscillations are present or absent. Some analysis of results will also be included. Throughout we use dimensionless quantities unless otherwise indicated for the reasons given below.

The size/shape of an osteocyte and dimensions of lacuna-canaliculi it lives in are highly variable but we have included some metrics for its main body and for its processes (see Section 2 above). Additionally, the lacuna has a mean volume of 290 ± 107 micron cubed [40], with the long-axis length in the range of 3 to 20 microns [24]. The canaliculi have diameters between 150 and 550 nanometers [40]. The gap between the cell body and lacunar wall is approximately 0.5 to 8.0 micron [40-42] , and between the process membrane and the canalicular wall is 78 ± 38 nm [43].

In literature, computational models of such a system typically assume the osteocyte and lacuna are in the shape of ellipsoids with different dimensions. For example, in [10, 18], the osteocyte is 7.5 μm x 7.5μm x 13.5μm and the lacuna is 9 μm x9 μm x15 μm. The processes and canaliculi are modelled as cylinders of diameters 0.44 μm and 0.6 μm, respectively. In [16], the processes and canaliculi have diameters 0.6 μm and 0.7 μm, respectively, and osteocytes of three different shapes/sizes are considered: a scalene ellipsoid (major to minor axis ratio 5/3), a prolate ellipsoid (with ratio 4/3) and a sphere. In [25] there is a 3.5 μm x 3.5μm x 5.5μm osteocyte and a 4.0 μm x 4.0 μm x 6.0 μm for the lacuna while diameters for the process tapered from 0.3 to 0.2 μm and those for the canaliculi tapered from 0.45 to 0.3 μm.

Given the level of variability in the dimensions of the osteocyte-lacuna-canaliculi system, it is challenging to construct an accurate model for a specific system due to lack of experimental data. Instead, we focus on a generic osteocyte-fluid in a lacuno-canalicular system and introduce a minimum integrative FSI model for such a system using the lattice-Boltzmann immersed-boundary framework. Lattice Boltzmann methods communicate with the real world SI units via dimensionless quantities such as the Reynolds number. Therefore, we used dimensionless quantities throughout the paper including fluid stress and solid strain. Given a specific system, the dimensional equivalent can be obtained from the dimensionless quantities reported. See details in the Discussion Section and sample dimensional stresses in Table 3 below.

5.1 *Fluid motion and solid deformation*

Fig. 3 illustrates the typical flow field, including vorticity contours (nondimensionalized), and osteocyte deformation for the case of static loading (non-oscillatory flow). The left panels correspond to relatively low levels for the elastic moduli (K_s and K_b equals 1.2 dyn/cm and 9e-10 dyn-cm, respectively). The right panels correspond to higher elastic moduli (K_s and K_b equals 12 dyn/cm and 9e-9 dyn-cm, respectively). In both cases Re = 0.01. Black arrows correspond to the flow velocity with the black arrow length indicating the velocity magnitude. Notice that arrows crossing the structure (ellipse or interior links) do not suggest fluid penetrating the structure; rather they represent velocities at points located close to the structure with the local structure moving at similar speeds and direction. The maximum speed in the system is around O(1e-5). The osteocyte membrane (red), processes (blue), and links/cytoskeleton (green) are plotted at the indicated times. Also included in black are the osteocyte components at its initial configuration. Comparing allows visualization of the deformations that the components of the cell typically undergo.

The figure further shows the effect of cell elasticity by allowing comparison between a more flexible (a) vs. a more rigid cell (b). In both cases, the cell experiences vertical compression and horizontal stretching and rotates counterclockwise, due to the flow entering the lacuna from north and south canaliculi and exiting to the west and east canaliculi. The deformation is most pronounced and discernable by eye at the 4 junction points on the osteocyte membrane where processes meet the cell body. Additionally, the cell with lower moduli undergoes more deformation at these locations. The tendency for the cell to rotate is most clearly evidenced by investigating the flow field.

The low moduli scenario additionally develops recirculation zones in the upper right and lower left regions of the lacuna and cell body. The high moduli scenario does not develop such recirculation regions and instead rotates more as a rigid body creating a flow field more typical of a single vortex. In both cases the flow fields significantly differ from fields generated by stationary rigid osteocytes (see [32]). While these simulations can be helpful for characterizing osteocyte deformations, the actual physiological flow fields may also depend on other factors such as tethers (including focal adhesions) [5] and cilia [14].

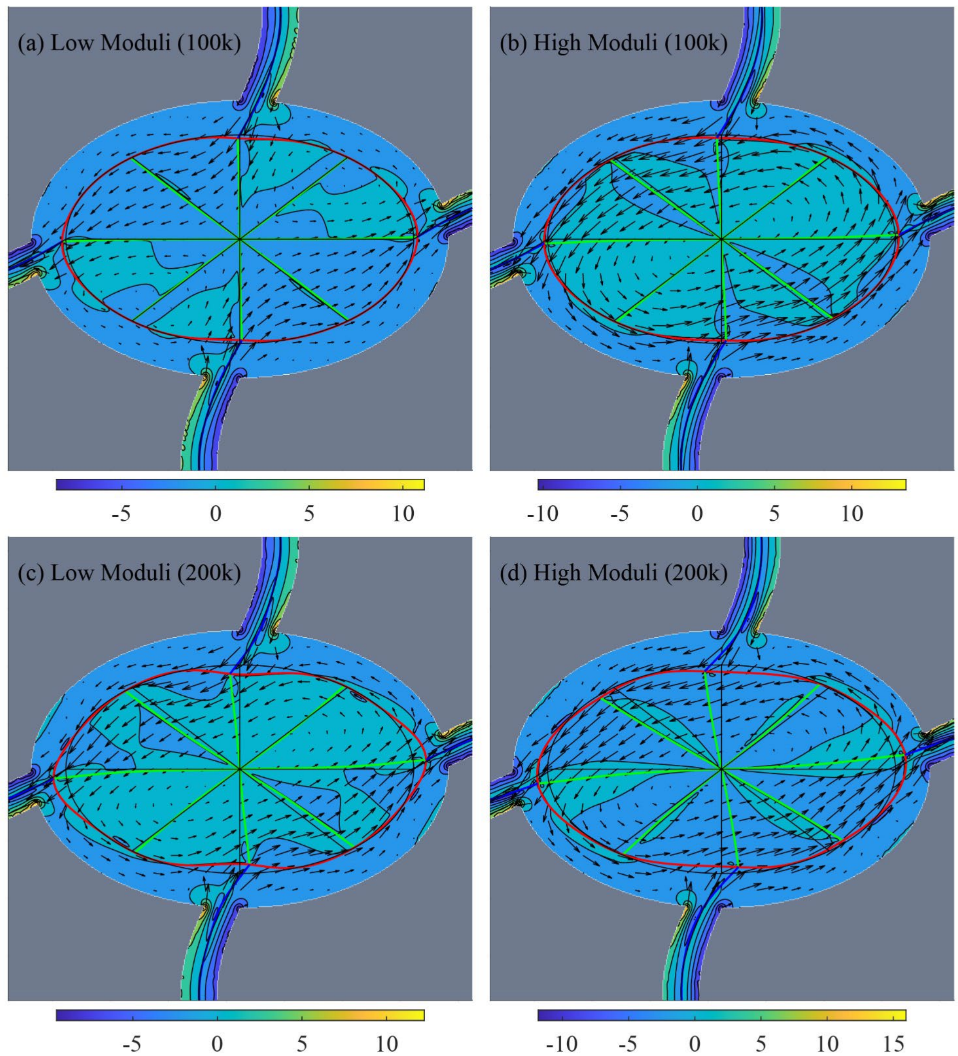

Fig. 3: Fluid motion (arrows) with vorticity (contours) and cell deformation (curves; static loading) for an osteocyte with low (a-c; $(K_s, K_b) =$ (1.2 dyn/cm, 9e-10 dyn-cm)) and high (b-d; $(K_s, K_b) =$ (12 dyn/cm, 9e-9 dyn-cm)) elasticities. Here, Re = 0.01. The graphs show the effects of more flexibility vs. more rigidity. We have included the processes (blue), links/cytoskeletal elements (green), and the membrane (red) at the indicated times. Black lines indicate the initial shape of the cell's components while black arrows correspond to the velocities at the indicated times. In both cases, deformation is largest in the cell membrane near the 4 junctions where processes meet the main body. Both cells rotate counterclockwise but generate substantially different flow fields: two local vortices in (a) and one vortex in (b).

Fig. 4 displays the typical flow field and osteocyte deformation for the cyclic loading case (oscillatory flow) over one cycle at 9 different times (a-i) starting at 600k timesteps with an increment of 50k timesteps. In the figure one can see the fluid flow and reverse directions. The frequency is 2e-6 cycles per LB time units, $Re = 0.1$, K_s, K_b values are the same as in Fig. 3 (case a-c). All symbols and colors have the same meanings as in Fig. 3. Velocity magnitudes here are typically O(1e-6).

Contrasting Figs. 3 and 4 allows us to better understand the differences that occur in this system in the presence of non-oscillatory vs. oscillatory flow. The absence/existence of flow reversal is relatively obvious. This causes more nontrivial behavior in the oscillatory case with inlets and outlets switching roles. Similarly, the osteocyte, which tends to undergo rigid body rotation, first rotates counterclockwise before reversing to the clockwise direction. This also causes the location of local vortices to alternate from being in the first and third quadrants to being in the second and fourth quadrants. Reversal similarly affects the deformation with the solid components experiencing maximum deformation approximately when the flow hits its maximal magnitudes and then going through periods of near-zero deformation as the flow changes direction. This has particular implications for where the membrane meets the processes. At those locations both local flow and processes push against or pull on the membrane creating relatively large stresses. In the case of oscillatory flow, this leads to particularly large swings in stresses at those junctions, which could serve as sources of temporally variable stimuli on the osteocyte membrane with potential implications for mechanotransduction.

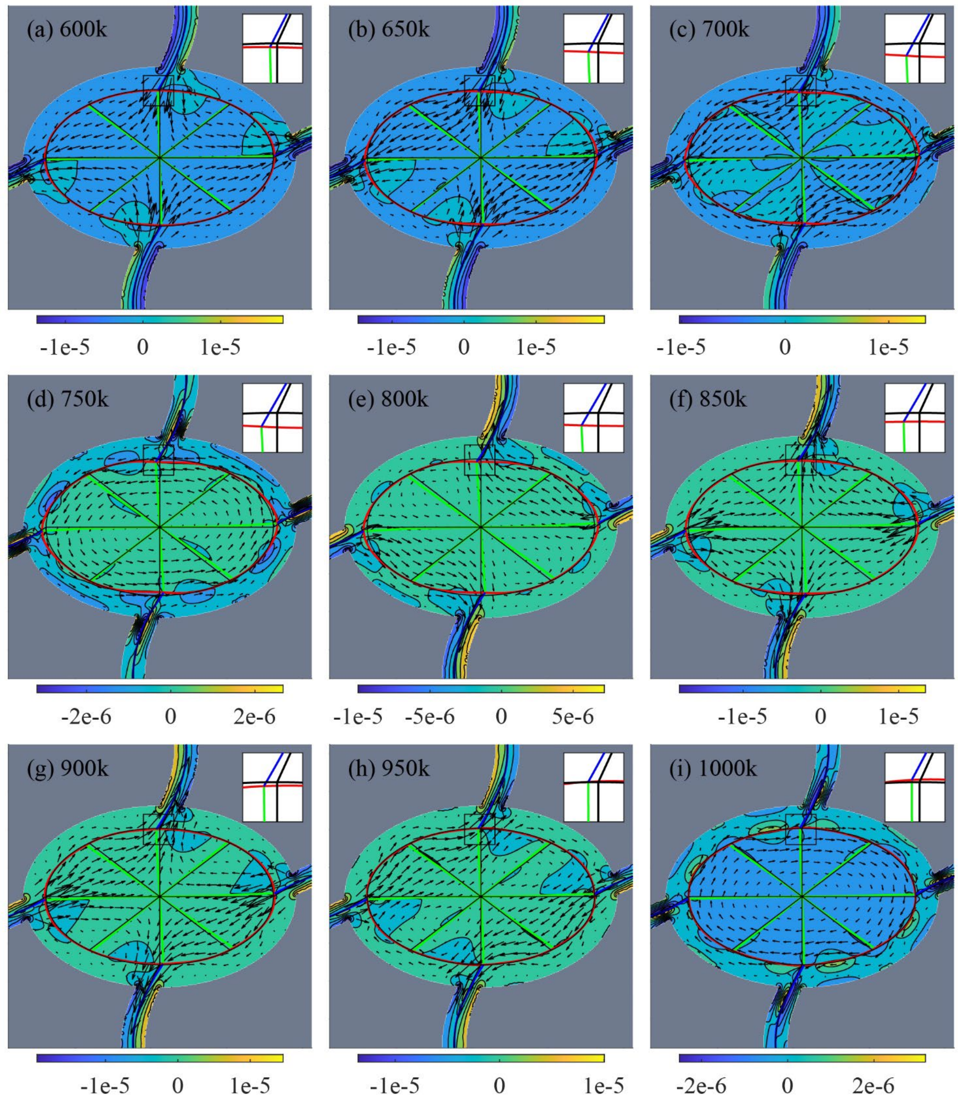

Fig. 4: Same as in Fig. 3 but with cyclic loading over one cycle. Loading frequency is 2e-6 in LB units with $Re = 0.1$ and K_s, K_b values are the same as in Fig. 3 (case a-c). One can see the typical dynamics as the fluid flows and then reverses directions over different timesteps (600-1000k; a-i). Insets near the upper membrane-link-process junction are also included. Maximal speeds are typically O(1e-6).

Fig. 5 Considers flow, particularly normalized speed (speed divided by inlet speed), in the process/canaliculi region (b-c) but also includes a deformed cell depicted using the entire computational domain (a). The simulation was made using non-oscillatory flow, Re, K_s, K_b values are the same as in Fig. 3 (case a-c) and integrated until 300k timesteps. The deformed cell components in Fig. 5(a) shows how processes tend to stay in the center of the canaliculi resulting in significantly less deviation of those components from the path of their initial configurations compared to the membrane and links. At the same time, Fig. 5 (b-c) shows that while the process remains roughly centralized in the canaliculus, it can still stretch out significantly along that pathway resulting in non-trivial forces within the process. The picture also highlights (red box) different speeds above and below the canaliculus that can occasionally give rise to forces that tend to twist the process.

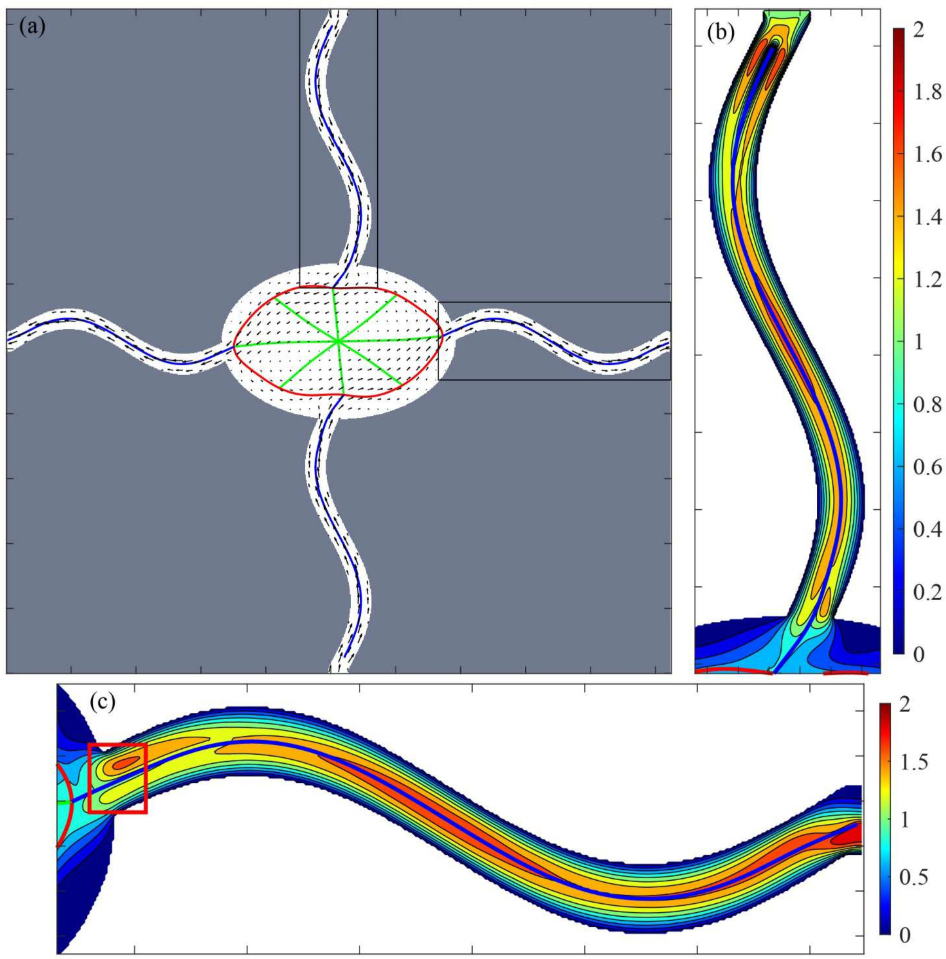

Fig. 5: Same as in Fig.3. (a) shows the general flow fields and deformation of a cell at 300k timesteps where Re, K_s, K_b values are the same as in Fig. 3 (case a-c). To better visualize flow in the osteocyte processes, we have zoomed in on the upper (b) and right (c) processes and plotted contours of the normalized speed (speed/inlet speed).

5.2 *Fluid stress on osteocyte*

Figs. 6-7 show typical stresses and other stress-related quantities exerted by the fluid on the osteocyte membrane and processes for both static (Fig. 6) and cyclic loadings (Fig. 7). In both figures, the stress on the membrane is given in terms of the polar angle, θ, which is a Lagrangian variable associated with the initial location of each point (x_0, y_0) on the membrane. The point where the eastern process meets the cell membrane corresponds to $\theta = 0$. Positive values of θ corresponds to counterclockwise and negative to clockwise. The stress on the processes is given in terms of the original distance that the point on the process is from the membrane, measured along the process (a Lagrangian variable). All quantities associated with the normal direction (vs. shear quantities) in Figs. 6-7 have been shifted so they have a mean of zero because pressure can always differ by an additive constant without affecting flow dynamics. Stresses in all plots are dimensionless.

The symmetry of our model renders the stresses in the top and bottom processes nearly equal (except for computational roundoff errors) as is the case for the right and left processes. Therefore, only the top and right processes have been plotted here. Of primary interest is the force exerted by the fluid on the membrane with higher forces corresponding to more likely sites for mechanosensory locations. For this reason, we present only the stress exerted by the extracellular fluid in the lacuna on the membrane while not showing the stresses that the fluid inside the cell exerts on the membrane. Similarly, we do not present stresses exerted by the fluid on the cytoskeleton.

The top and bottom processes are tethered at fixed points near the north and south boundaries and experience larger stresses there due to that tethering. Such tethering is not as physiologically realistic compared to connecting the processes to other cells. Similarly, at the outlets, the processes are assumed free instead of connected to other cells. Because of this, results at the ends of the processes (c-j in Figures 6-7) are not focused on in this study.

On the outside of the osteocyte membrane, a positive value of $f_n = \hat{\mathbf{n}} \cdot \boldsymbol{\sigma} \cdot \hat{\mathbf{n}}$ ($\hat{\mathbf{n}}$ is the unit outward normal vector and $\boldsymbol{\sigma}$ is the stress tensor for the external fluid) corresponds to the external fluid pulling directly outward on the process while a positive value for $f_t = \hat{\mathbf{t}} \cdot \boldsymbol{\sigma} \cdot \hat{\mathbf{n}}$ ($\hat{\mathbf{t}}$ is the unit tangential vector along the membrane pointing anticlockwise) corresponds to external fluid pulling in a counterclockwise fashion. f_t is usually positive, which is consistent with Fig. 3 where the fluid tends to rotate the cell counterclockwise.

For the processes, fluid exerts forces on both sides of a given process. We denote the left side of the top process and the top side of the right process as the "positive" (+) side (where $\hat{\mathbf{n}}$ points to) with the other side denoted as "negative" (-) side (where -$\hat{\mathbf{n}}$ points to). We also define a unit tangent vector pointing outward (away from the cell's main body) along the process curve as $\hat{\mathbf{t}}$. We denote the stress tensor of the fluid on the positive side by σ_+ and on the negative side by σ_-. Then $\boldsymbol{\Sigma}_+ = \boldsymbol{\sigma}_+ \cdot \hat{\mathbf{n}}$ gives the force exerted by the fluid on the positive side on the process while $\boldsymbol{\Sigma}_- = \boldsymbol{\sigma}_- \cdot (-\hat{\mathbf{n}})$ gives the force exerted by the fluid on the negative side on the process. To facilitate analysis, we let $\bar{\boldsymbol{\Sigma}} = \boldsymbol{\Sigma}_+ + \boldsymbol{\Sigma}_-$ be the total force acting on the process which drives the motion of the process, including motion along the process (tangential stress $\bar{f}_t = \hat{\mathbf{t}} \cdot \bar{\boldsymbol{\Sigma}}$; positive means outward) and perpendicular to the process (normal stress $\bar{f}_n = \hat{\mathbf{n}} \cdot \bar{\boldsymbol{\Sigma}}$; positive means force towards the "positive" side).

Accepted to Phys. Fluids 10.1063/5.0165467

We further consider the difference in the forces across the process, namely let $\boldsymbol{\Delta\Sigma} = \boldsymbol{\Sigma}_+ - \boldsymbol{\Sigma}_-$ be the difference between the forces on both sides. The normal component of the difference, $\Delta\Sigma_n = \hat{\mathbf{n}} \cdot \boldsymbol{\Delta\Sigma}$, tells us how much the process is being pulled apart by the fluid on the positive and negative side. Alternatively, $-\Delta\Sigma_n$ tells how much the process is being compressed by the fluid on the positive and negative side (akin to how a deep diver can feel compressed by the surrounding ocean). Further, since the variation of pressure is significantly larger than variations in the deviatoric stress components, $\boldsymbol{\sigma}_\pm = \left(\mu(\mathbf{u}_{\pm i,j} + \mathbf{u}_{\pm j,i})/2 - \delta_{ij}p_\pm\right) \approx -\delta_{ij}p_\pm$ so that $-\Delta\Sigma_n \approx (p_+ + p_-) = 2p_{ave}$. This corresponds to pressure squeezing the process from both sides. Differences in the tangential components, $\Delta\Sigma_t = \hat{\mathbf{t}} \cdot \boldsymbol{\Delta\Sigma}$, tells about the tendency for the process to experience torque or local deformation caused by shear stresses that differ significantly on the positive vs. negative side. As it is not entirely clear which of these stress-related quantities is best suited for mechanosensation, we have included them all in our plots and discussion.

Panels (a) and (b) plot the normal and shear stress exerted by the external fluid on the membrane versus the angle θ. Both normal and shear stress magnitudes peak at the four conjunction points (θ = 0, 0.5π, -0.5π, π) indicating that regions where processes meet the cellular main body may be good mechanosensory site locations.

Panels (c-f) plot the total normal and shear stress exerted by the interstitial fluid on the processes in the eastern (c-d) and northern canaliculi (e-f). The stress distributions for the two processes look similar, especially near the conjunctions where they are attached to the cell body (sign difference because of different flow direction). This might indicate that it does not matter much whether the fluid flows in or out of a canaliculus for the purpose of mechanotransduction. The regions near where the processes meet the cellular body experience the highest normal and shear stresses from the interstitial flow. The middle parts of the processes feel relatively little stress. These trends again suggest that the parts of the processes close to the cell body may be good mechanosensory site locations.

Panels (g-j) plot the differences in stresses on two sides of the processes for the right process (g-h) and top process (i-j). We see that both normal and shear stress differences look similar for the two processes except for the sign due to different flow direction. Secondly, the amount the processes being squeezed ($-\Delta\Sigma_n > 0$) drops as one travels along the direction of flow (left to right for the right process and top to bottom for the top process). This is consistent with the typical trend of dropping pressure as one travels down a flow pathway ($-\Delta\Sigma_n \approx -2p$). For the $\Delta\Sigma_t$ plots, flows that are faster on one side of the process and slower on the other side tend to generate torques. Looking at the speed plots in Fig. 5, for instance, show that near the membrane (red box) there is a red high velocity region above the process and a lower velocity region below the process yielding a tendency for the process to rotate clockwise. This corresponds to the large positive region near 50 units on Fig. 6(h).

Our simulation results also show that both the normal and shear stresses from the interstitial flow on processes are typically smaller in magnitude than those on the cell membrane, especially near the four junction points.

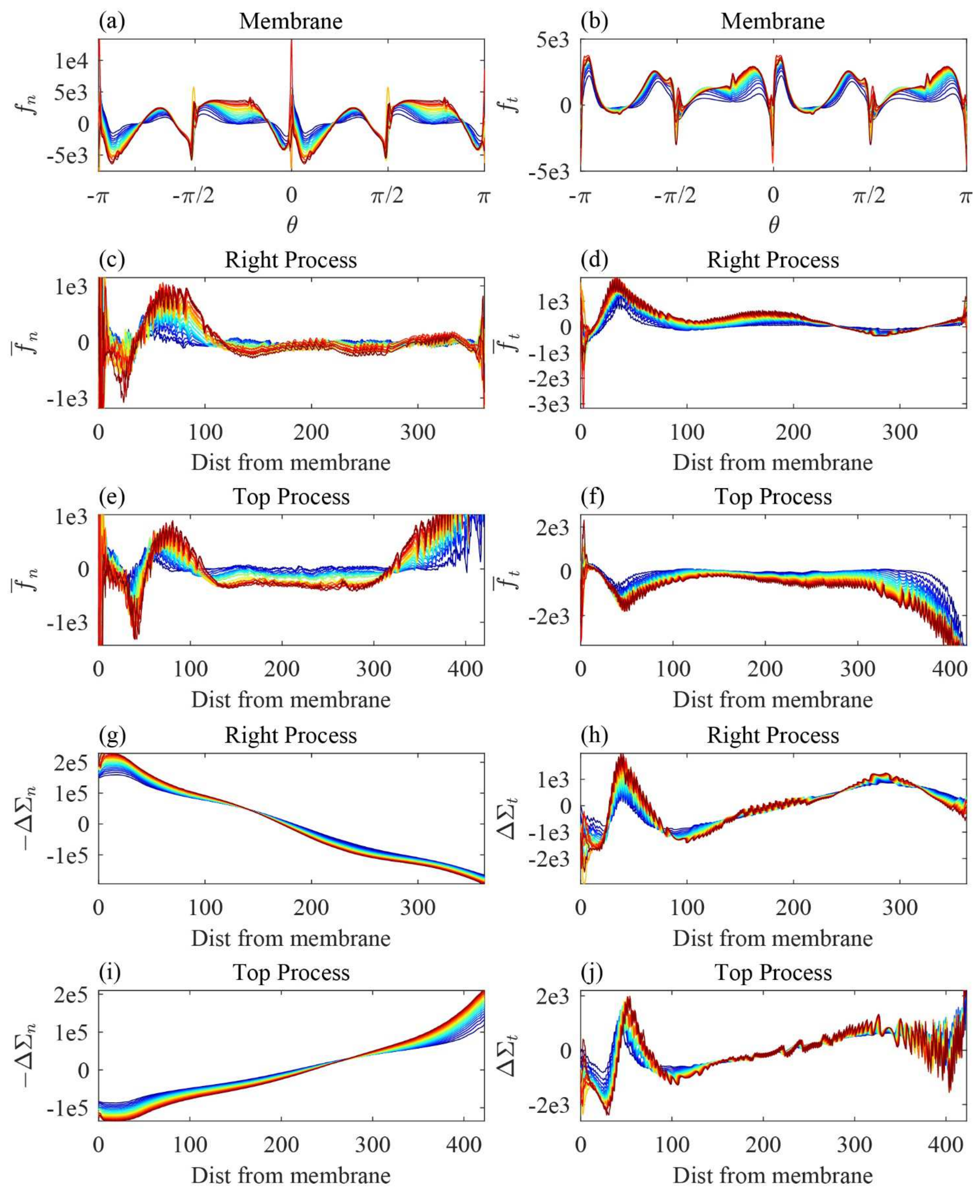

Fig. 6: Non-dimensional fluid stress-related quantities (static loading). The figure plots normal and shear forces exerted by the extracellular fluid on the cellular membrane (a-b) and the right (c-d) and top (e-f) processes. Colors represent multiple times starting from purple at time 50k and heading through blue, green, yellow, orange, and then dark red at time 1000k with 50k between each displayed time. Panels (g-j) correspond to stress-related quantities that correspond to the tendency for the fluid to compress ($-\Delta\Sigma_n > 0$) or twist clockwise ($\Delta\Sigma_t > 0$) the processes. Re = 0.001 and $(K_s, K_b) =$ (1.2 dyn/cm, 9e-10 dyn-cm) for all osteocyte components.

Fig. 7 plots the non-dimensional normal and shear stresses and other stress-related quantities on the osteocyte for the cyclic loading case (oscillatory flow). The loading frequency is 2e-6 cycles/timestep, Re = 0.001, and $(K_s, K_b) =$ (1.2 dyn/cm, 9e-10 dyn-cm)). The plot considers stresses exerted by the interstitial fluid on the cell's membrane and processes. Colors represent different times starting from blue at time 550k and heading through green, yellow, orange, and then dark red at time 1000k with 50k between each displayed time. Panels (a-b) correspond to the stresses on the membrane, (c-d) correspond to stresses on the right process, and (e-f) correspond to stresses on the top process. Panels (g-j) correspond to how much the process is compressed ($-\Delta\Sigma_n > 0$) or subjected to clockwise twisting stresses ($\Delta\Sigma_t > 0$).

Compared to the static case, the fluid normal and shear stresses on the membrane and processes are all oscillatory in line with the oscillation of the interstitial flow induced by cyclic loading. The forces experience approximate periodicity and repeat every 500k timesteps. The distributions of the forces at the last instant, the peak of the loading cycle, tend to approach the steady state behavior corresponding to the static loading case. During the oscillations, however, the system undergoes approximate reversal with forces again approaching the steady state distributions but with a negative sign. As oscillatory loading has been seen to affect cells differently than steady loading [44], this kind of oscillatory forcing on the osteocyte may generate stronger mechanical cues for mechanosensation despite lower average stresses and stress-related quantities for the same Reynolds number. We also point out that the oscillations do not repeat exactly from cycle to cycle, instead there is a spatially dependent lag in time. This is possibly caused by the viscoelasticity of the osteocyte-fluid system which consists of an elastic osteocyte and a viscous fluid.

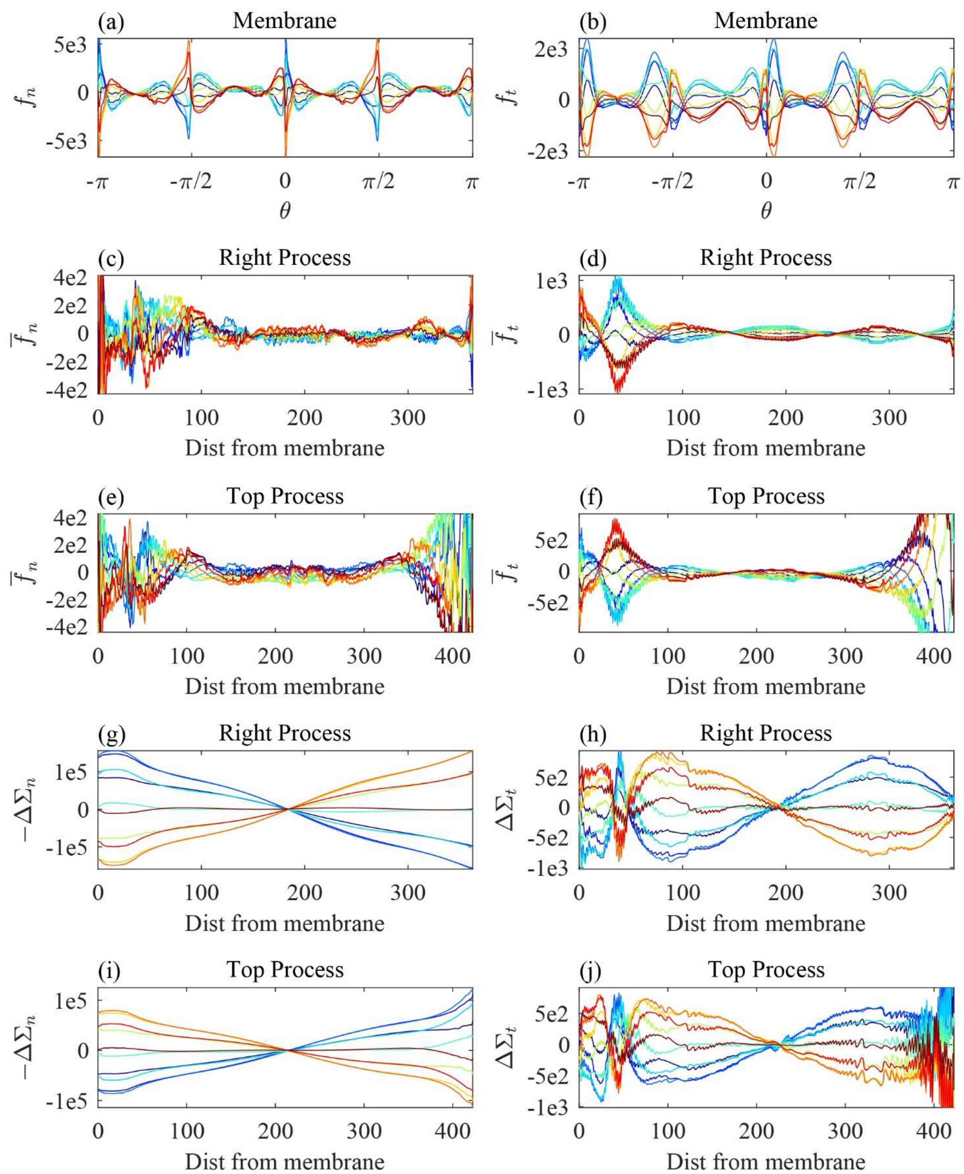

Fig. 7: Non-dimensional fluid stresses and stress-related quantities (cyclic loading, oscillatory flow). The loading frequency is 2e-6 cycles per timestep, Re = 0.001, and $(K_s, K_b) =$ (1.2 dyn/cm, 9e-10 dyn-cm)). The panels show the stresses (and stress-related quantities) the interstitial fluid exerts on the cellular membrane and processes. Colors represent different times starting from purple at time 550k and heading through blue, green, yellow, orange, and then dark red at time 1000k with 50k between each displayed time. Panels (a-b) correspond to the forces on the membrane. Panels (c-

d) correspond to forces on the right process. Panels (e-f) correspond to forces on the top process. Panels (g-j) correspond to differences between the stresses on both sides on the processes representing process compression (g,i) and clockwise twisting (h,j; see text).

Spatial oscillations in fluid stresses and related stress quantities are observed in Figs. 6 and 7 (zigzags on curves), in particular along processes. While using radial basis functions provides some level of smoothing, there are still a significant number of factors that are probably causing such oscillations. One factor is the relatively low level of refinement in the canalicular region. The canaliculus is 32 lattice units across making the process 16 units or less from the rigid wall at any given time. Additionally, the rigid wall is approximated using a stair-step pattern. On the theoretical side, the shear stress across a channel filled with fluid can vary greatly, in a relative sense, with maximal values at the walls and zero shear stress at the center. Our simulations show that the process is near the center and tends to experience relatively low stresses compared to elsewhere in the channel so that we are often trying to approximate near zero stresses use O(1) stress values, which can lead to large relative errors. Similar oscillations can be seen for the membrane but they are smaller. The membrane is farther from the wall and also does not suffer from issues of approximating near zero stresses. The membrane experiences relatively high magnitude stresses, compared to the process, as flow impinges or pulls away from the membrane.

5.3 *Strain on osteocyte*

Fig. 8 plots the difference $l - l_0$, κ, and κ_0 as functions of either θ, the polar angle along the ellipse, or the initial distance from the membrane along the process. $l - l_0$ between any two points on the solid components is given by the current distance between the two points (l) minus the initial/reference distance between the two points ($l_0 = d\alpha$). κ is the current curvature of a line segment and κ_0 is the initial curvature. The quantity $l - l_0$ gives an indication of the amount of strain and resulting tension felt in the solid component. Comparing κ vs. κ_0 allows us to understand how much the solid components have been bent, which gives rise to forces withing the component that resist that bending motion. In Fig. 8, the parameters used are Re =0.01 and $(K_s, K_b) =$ (1.2 dyn/cm, 9e-10 dyn-cm)). Left panels plot $l - l_0$ and right panels plot the current and reference curvatures. As before, colors denote times starting from 50k and going by 50k to 1000k with dark black denoting κ_0 in the right panels. Panels (a-b) correspond to the elliptical membrane, (c-d) to the right process, and (e-f) to the top process.

The membrane mostly experiences positive tension. Circles minimize the perimeter-area ratio while more elongated shapes have higher perimeter-area ratios. In our non-oscillatory case, the cell is compressed so that it becomes more elongated. At the same time, the cell is filled with incompressible fluid so that its area is approximately conserved. In order to maintain a constant area while allowing for elongation, the cell's perimeter must increase. This produces mostly positive tensions in the membrane. At the same time, due to the top and bottom processes ($\theta = \pm\frac{\pi}{2}$) pushing on the cell in a counter-clockwise fashion and the membrane in turn pushing the right and left processes ($\theta = 0$ and π) outwards, portions of the membrane near the membrane-link-process junctures are under compression. At the juncture, there are discontinuities in the tension as all three solid components make their contributions. Similarly, around $\theta = \pm\frac{3\pi}{4}, \pm\frac{\pi}{4}$, kinks can be seen as links connect to the membrane.

The squeezing motion flattens the top and bottom of the membrane causing the curvature to head towards zero before the curve inverts itself and the curvature grows in the positive direction. The squeezing motion also increases the curvature magnitude at the left and right of the ellipse driving it further in the negative direction.

The right/left processes are, on average, pulled towards the exit, which creates larger positive tensions near the juncture. This produces the mostly positive tensions across the process. At the same time, as seen in Fig. 5, the straight portion of the canaliculus seems to experience higher average velocities near its centerline. This causes the portion of the process in the straighter portion to be accelerated towards the slower moving portion of the process in the curved portion of the canaliculus near the exit. This produces compressed process material as the straight region blends into the curved region. There are at least two possible reasons why there tends to be higher velocities in the straighter portion and lower velocities in the curved portion. First, as straight process material enters the curved region, it takes energy to bend the process, which may take away from the kinetic energy in the region and slow material down. Second, fluid more readily flows through straight vs. curved portions of the canaliculi due to the fluid slowing down as it is redirected.

The top/bottom process is pulled from where it is anchored near the entrance towards the membrane. This produces tension near that anchor point and compression as the process pushes the membrane in a counterclockwise fashion near the membrane.

In the processes, the general counterclockwise rotation of the ellipse causes significant deviations of the curvature from its initial/reference values near the membrane. Otherwise, the curvature only seems to shift corresponding to the processes approximately following the centerlines of the canaliculi as they travel either towards (top/bottom process) or away from (left/right process) the membrane.

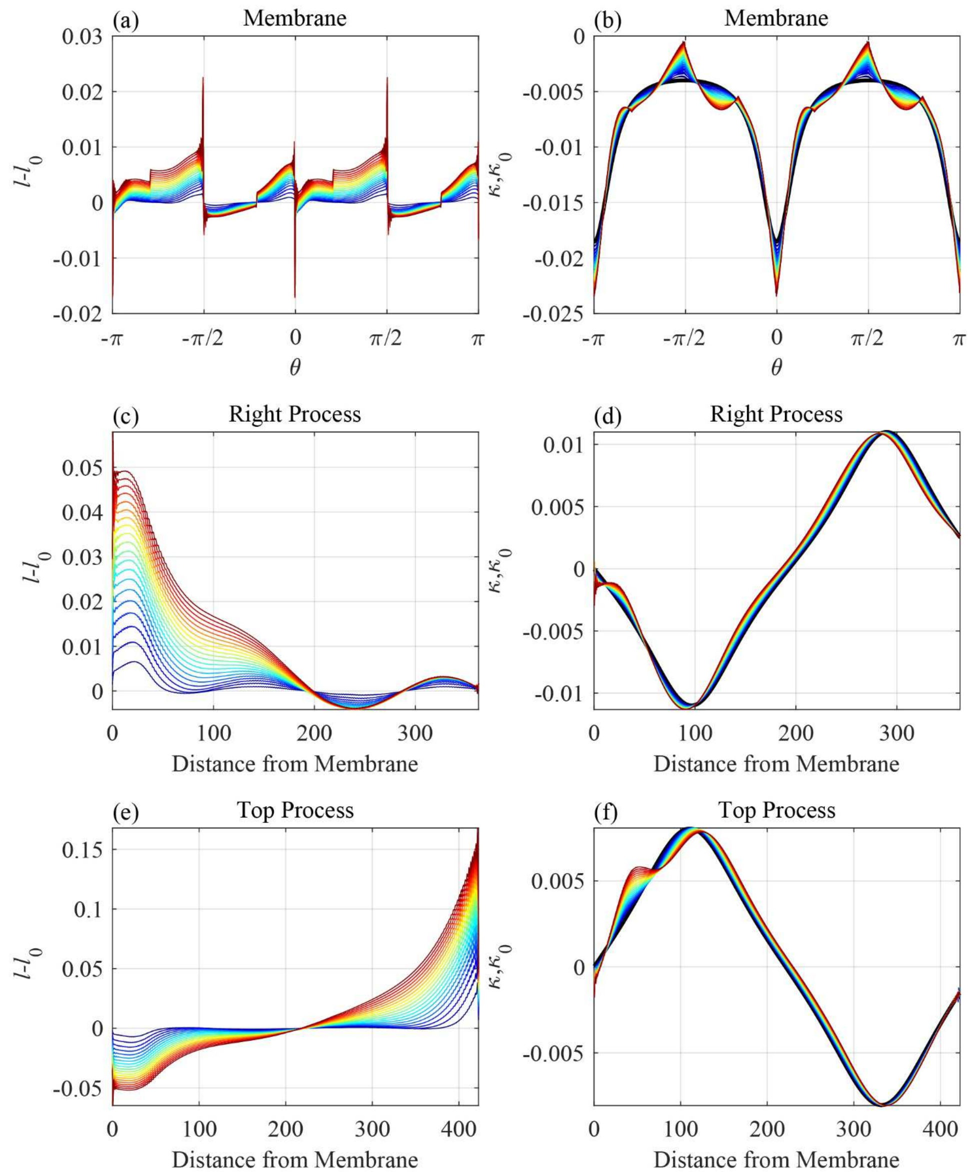

Fig. 8: Stretching (a,c,e) and bending (b,d,f) in the solid components (static loading, non-oscillatory) along the membrane (a-b), right process (c-d), and top process (e-f). The Re =0.001 and $(K_s, K_b) =$ (1.2 dyn/cm, 9e-10 dyn-cm)). Colors denote different time instants as in Fig. 6 varying from 50k to 1000k with 50k timesteps in between each. The first row plots the change in length (stretch, left panel) and the current and initial/reference curvatures (right panel; initial curvature is black) on the cellular membrane. The second and third row plot the same quantities on the right and top process, respectively.

Fig. 9 plots stretching and bending for cyclic loading with oscillatory flow. Here, the loading frequency is 2e-6 cycles per timestep, Re = 0.1, and $(K_s, K_b) =$ (1.2 dyn/cm, 9e-10 dyn-cm)). Colors denote different times as in Fig. 7, starting from purple at 550k timesteps and heading through blue, green, yellow, orange, and then dark red at time 1000k with 50k between each displayed time. Left panels plot the change in length or stretch while the right panels plot the current and initial/reference curvature (reference curvature in black). The first, second, and third rows plot the cellular membrane, right process, and top process, respectively. For a given time instant, the strain distributions on the osteocyte have the same features as in the static case.

In contrast with the stresses in Figs. 6-7, here the stretch and curvatures for these oscillatory cases exhibit features not seen in the non-oscillatory scenario. For instance, in Fig. 9(a), a discontinuity in the stretch appears where the links attach to the membrane. In the steady state case there is only a moderate kink at those locations. Similarly, due to lag as the velocity changes directions, the stretches and curvatures look more oscillatory in general. Stretching and bending are again smaller, probably due to the reversibility phenomenon, i.e. that the deformations approximately reverse themselves as oscillations proceed so that larger deformations not given sufficient time to develop.

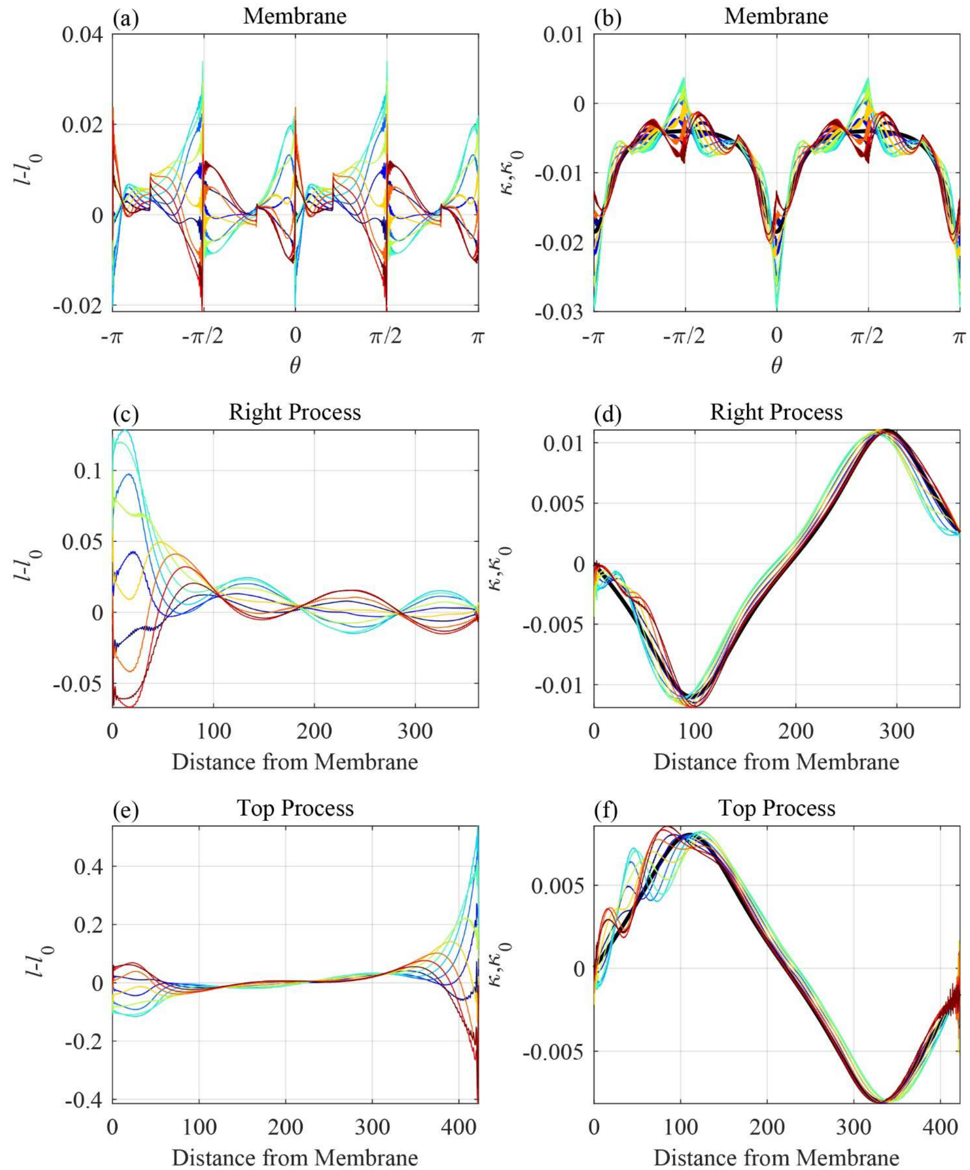

Fig. 9: Stretching (a,c,e) and bending (b,d,f) in the solid components (cyclic loading, oscillatory flow) along the membrane (a-b), right process (c-d), and top process (e-f). Here, $Re = 0.01$, $(K_s, K_b) =$ (1.2 dyn/cm, 9e-10 dyn-cm)), and the loading frequency is 2e-6 cycles per timestep. Colors denote different time instants as in Fig. 7 starting with purple at time 550k and heading through blue, green, yellow, orange, and then dark red at time 1000k with 50k between each displayed time. The first row plots the relative change in length (strain, left panel) and in curvature (right panel) on the cellular membrane. The second and third row plots the same quantities on the right and top process, respectively.

Fig. 10 plots dimensionless average stress for the cyclic loading per unit length (and per unit along the z direction; with dimension being force/length^2) for all simulations considered in a factorial study as functions of time (in LB units) for the cell membrane (red), cytoskeleton/links (green), and processes (blue). The loading frequency is 5e-6 cycles per timestep. The factorial study uses high (red text in title on top of each panel) and low (blue text in title) values of elasticities for the cellular membrane, cytoskeleton/links, and processes. Reynolds numbers used are 1.0e-3 and 1.0e-4. The stretching and bending elastic moduli for each cellular component (membrane, cytoskeleton, and processes) are always changed together, simultaneously. For less rigid scenarios, $(K_s, K_b) =$ (1.2 dyn/cm, 9e-10 dyn-cm). For more rigid scenarios, $(K_s, K_b) =$ (12 dyn/cm, 9e-9 dyn-cm). The elastic moduli are adjusted in this paired fashion independently for the internal links (l), i.e. cytoskeleton, the membrane (m), and the processes (p).

In general, because the solid components are interconnected, changing just the elastic moduli on just one of the components tends to affect stresses on the other components as well. For instance, increasing the elastic moduli of the links (left half vs. right half) seems to increase the stresses generated by the links but also increases the stresses generated in the other solid components. The plots show how the average stress can wax and wane as the oscillations take place, which is significantly different from the non-oscillatory case (not shown) where the average stresses continuously grow over time. The plots also show that the membrane forces tend to be larger than the others over all cases, consistent with previous figures.

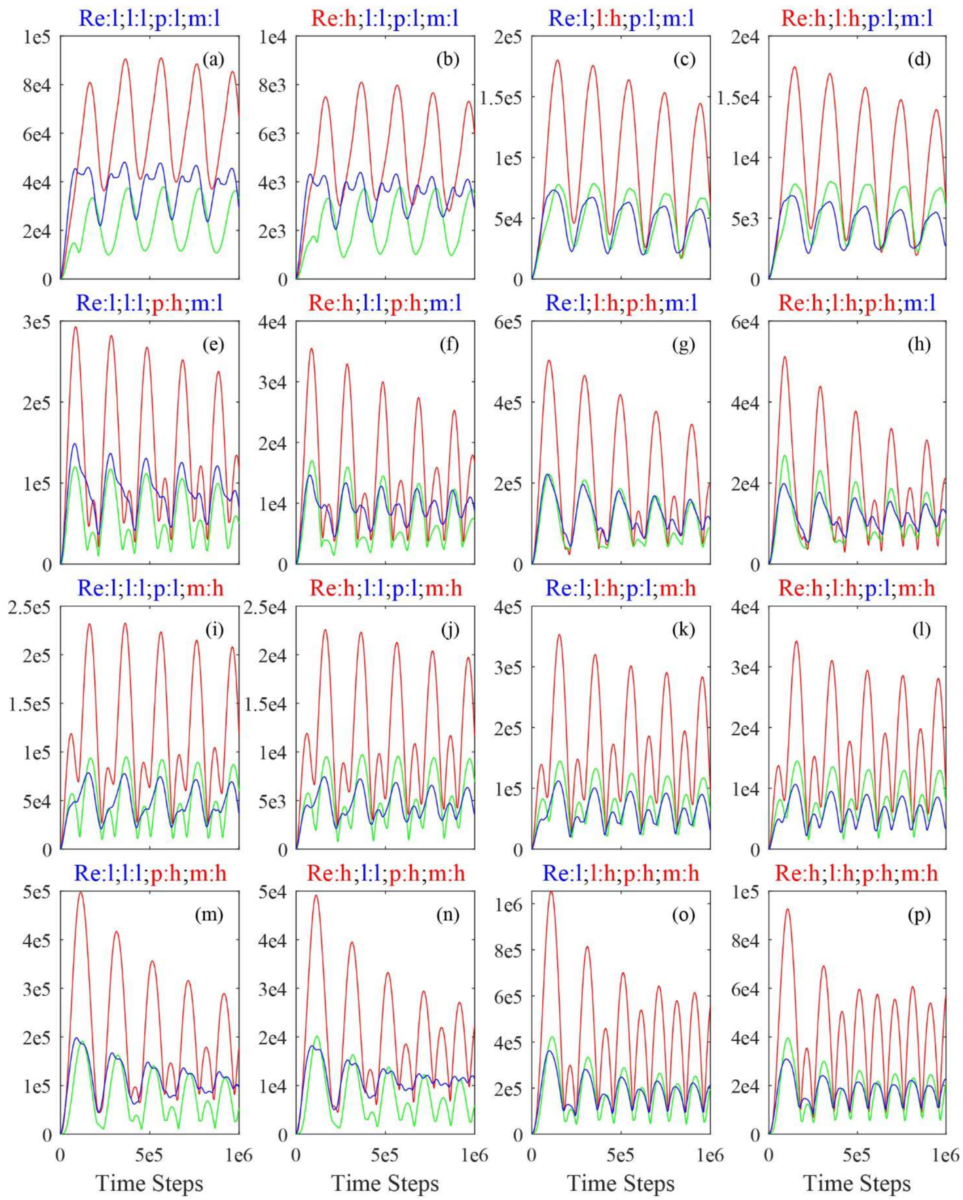

Fig. 10: Dimensionless average force per unit length (and per unit along z direction; with dimension being force/length^2) for all simulations (a-p) considered in the factorial study as functions of time (in LB units) for the cell membrane (red), cytoskeleton (green), and processes (blue). Low values (denoted by "l") of the factors (Reynolds number (Re), link elastic moduli (denoted by "l"), process elastic moduli (denoted by "p"), and membrane elastic moduli (denoted by "m")) are shown as blue in the title while high values (denoted by "h") are shown as red in the title bar.

To better quantify differences between low and high factorial values, oscillation speeds (or lack thereof), and stress locations (links, processes, membrane), we have tabulated average dimensionless stresses. In the averaging procedure, we first found the average link, process, and membrane stresses for a given simulation in the factorial study for all time. For links and processes, the stresses were additionally averaged over all 8 links and all 4 processes. To facilitate comparison, we then separated the simulations into non-oscillatory, low oscillatory (2e-6 cycles per timestep), or high oscillatory (5e-6 cycles per timestep) cases. This gives sixteen simulations for each of those three cases. Within the groups of sixteen, we then averaged the stresses over high and low factor levels for each factor to produce estimates for the low and high mean stresses when each factor was changed. Additionally, we found the differences between the stresses for each simulation in the following way: $\Delta_{ijk} = \bar{\mu}_{2ijk} - \bar{\mu}_{1ijk}$ where 2 and 1 correspond to the high and low level of the factor of interest and i, j, and k vary from 1 to 2 and correspond to the levels of the other factors. Such differences compare simulations that only differ in the one factor of interest while the other factors are held constant. We then did a one-sample t-test on these differences (Matlab ttest) to obtain a p-value telling us how likely it is that the differences differ from zero. As results suggest higher factors always produce more stress, the p-value effectively indicates which factors display more of an effect (smaller p-value) compared to other factors.

Those results in Table 2 more clearly show trends. As oscillation increases, the average stresses experienced decrease for all solid components. Membrane stresses are typically at least twice the stresses in links and processes. Links tend to have higher stresses than processes, but that trend diminishes as oscillation frequency is increased.

To understand the rest of the results on the table 2 more clearly, consider just the 3×4 "Link Stresses" and "Non-Oscillator" box. The average stress on the links for the low Reynolds number (Re) is just 2.4e-7 while it is 2.8e-6 for the high Reynolds number. The relatively small p-value of 0.0037 suggests a strong tendency for an increased Reynolds number to yield increased stresses. In contrast, the average stress on the links for low membrane elastic moduli is 1.4e-6 while for high membrane elastic moduli it is 1.7e-6. The larger p-value suggests a weaker dependency of the average stress on the membrane elastic moduli. Looking across the table 2 suggests that increasing the Reynolds number or elastic moduli will always tend to increase the average stresses experienced in the system.

	Factors	Non-Oscillatory			Low (2e-6) Frequency			High (5e-6) Frequency		
		Low	High	p-value	Low	High	p-value	Low	High	p-value
Link Stresses	Re	7.70E+05	9.10E+04	0.0017	1.80E+05	2.00E+04	0.0043	7.70E+04	8.00E+03	0.0023
	Links	3.00E+05	5.60E+05	0.017	6.40E+04	1.30E+05	0.043	2.90E+04	5.60E+04	0.046
	Processes	2.50E+05	6.20E+05	0.021	5.60E+04	1.40E+05	0.04	2.70E+04	5.70E+04	0.037
	Membrane	4.00E+05	4.70E+05	0.17	7.70E+04	1.20E+05	0.079	3.30E+04	5.20E+04	0.049
Avg		4.30E+05			9.90E+04			4.20E+04		
Process Stresses	Re	6.40E+05	5.90E+04	0.0011	1.80E+05	1.50E+04	0.0025	8.70E+04	8.50E+03	0.0016
	Links	2.90E+05	4.10E+05	0.046	7.70E+04	1.20E+05	0.08	4.00E+04	5.60E+04	0.08
	Processes	2.00E+05	5.00E+05	0.025	5.10E+04	1.40E+05	0.034	2.60E+04	6.90E+04	0.024
	Membrane	3.10E+05	3.90E+05	0.12	7.80E+04	1.10E+05	0.094	4.00E+04	5.50E+04	0.07
Avg		3.50E+05			9.60E+04			4.80E+04		

Membrane Stresses	Re	1.70E+06	1.80E+05	0.0012	4.20E+05	4.00E+04	0.0053	1.80E+05	1.70E+04	0.003
	Links	7.50E+05	1.20E+06	0.027	1.70E+05	2.90E+05	0.078	7.30E+04	1.30E+05	0.08
	Processes	5.50E+05	1.40E+06	0.026	1.20E+05	3.30E+05	0.053	6.10E+04	1.40E+05	0.043
	Membrane	8.20E+05	1.10E+06	0.13	1.70E+05	2.90E+05	0.086	7.10E+04	1.30E+05	0.054
Avg		9.50E+05			2.30E+05			9.90E+04		

Tab. 2: Comparison of average dimensionless stresses for different factors (Reynolds number (Re), oscillatory frequency, and link, process, and membrane elastic moduli) and for the three solid components (links, processes, and membrane). Also included are average values of the indicated stresses across all simulations for each frequency-component pair, an average over 16 simulations.

	Factors	Non-Oscillatory			Low (2e-6) Frequency			High (5e-6) Frequency		
		Low	High	p-value	Low	High	p-value	Low	High	p-value
Link Stresses	Re	7.70E+00	9.10E+01	0.0037	1.80E+00	2.00E+01	0.0055	7.70E-01	8.00E+00	0.0015
	Links	3.10E+01	6.80E+01	0.038	7.00E+00	1.50E+01	0.053	3.00E+00	5.80E+00	0.045
	Processes	2.80E+01	7.00E+01	0.036	5.80E+00	1.60E+01	0.041	2.90E+00	6.00E+00	0.033
	Membrane	4.50E+01	5.40E+01	0.2	9.10E+00	1.30E+01	0.05	3.60E+00	5.20E+00	0.054
Avg		4.90E+01			1.10E+01			4.40E+00		
Process Stresses	Re	6.40E+00	5.90E+01	0.00093	1.80E+00	1.50E+01	0.0028	8.70E-01	8.50E+00	0.0017
	Links	2.70E+01	3.80E+01	0.031	6.90E+00	1.00E+01	0.058	3.90E+00	5.50E+00	0.072
	Processes	1.90E+01	4.60E+01	0.019	4.50E+00	1.30E+01	0.027	2.50E+00	6.90E+00	0.022
	Membrane	2.90E+01	3.60E+01	0.093	6.90E+00	1.00E+01	0.082	4.00E+00	5.40E+00	0.069
Avg		3.20E+01			8.60E+00			4.70E+00		
Membrane Stresses	Re	1.70E+01	1.80E+02	0.002	4.20E+00	4.00E+01	0.0065	1.80E+00	1.70E+01	0.0025
	Links	7.20E+01	1.20E+02	0.038	1.60E+01	2.80E+01	0.068	7.20E+00	1.20E+01	0.078
	Processes	5.60E+01	1.40E+02	0.029	1.10E+01	3.30E+01	0.041	5.90E+00	1.30E+01	0.034
	Membrane	8.40E+01	1.10E+02	0.12	1.60E+01	2.80E+01	0.068	6.80E+00	1.20E+01	0.055
Avg		9.70E+01			2.20E+01			9.60E+00		

Tab. 3: Table of comparisons using *dimensionalized* average stresses (N/m^2) for different factors, with no other differences compared to the previous table 2.

Because table 2 does not include time dependency, Fig. 11 shows the median, maximum, and minimum values of the membrane (red), link/cytoskeleton (green), and process (blue) stresses as functions of time. (Fig. 11(c) also serves as a summary of Fig. 10 with (a-b) serving as similar summaries for lower frequency and non-oscillatory cases.) The means, maximums, and minimums are found over all sixteen simulations for a given oscillation setting (none, low, or high frequency). The plots show that the trends suggested by table 2 are, in general, relatively consistent over time. This includes higher membrane stresses and lower stresses as oscillation frequency increases. Still, the plots show additional results not available on table 2. For instance, the stresses in the links in the non-oscillatory case start out lower than those for the processes but eventually increase in magnitude relative to the processes so that they are higher than the process stresses towards the end of the simulation. This shift in relative strengths is not shown by the table 2.

Accepted to Phys. Fluids 10.1063/5.0165467

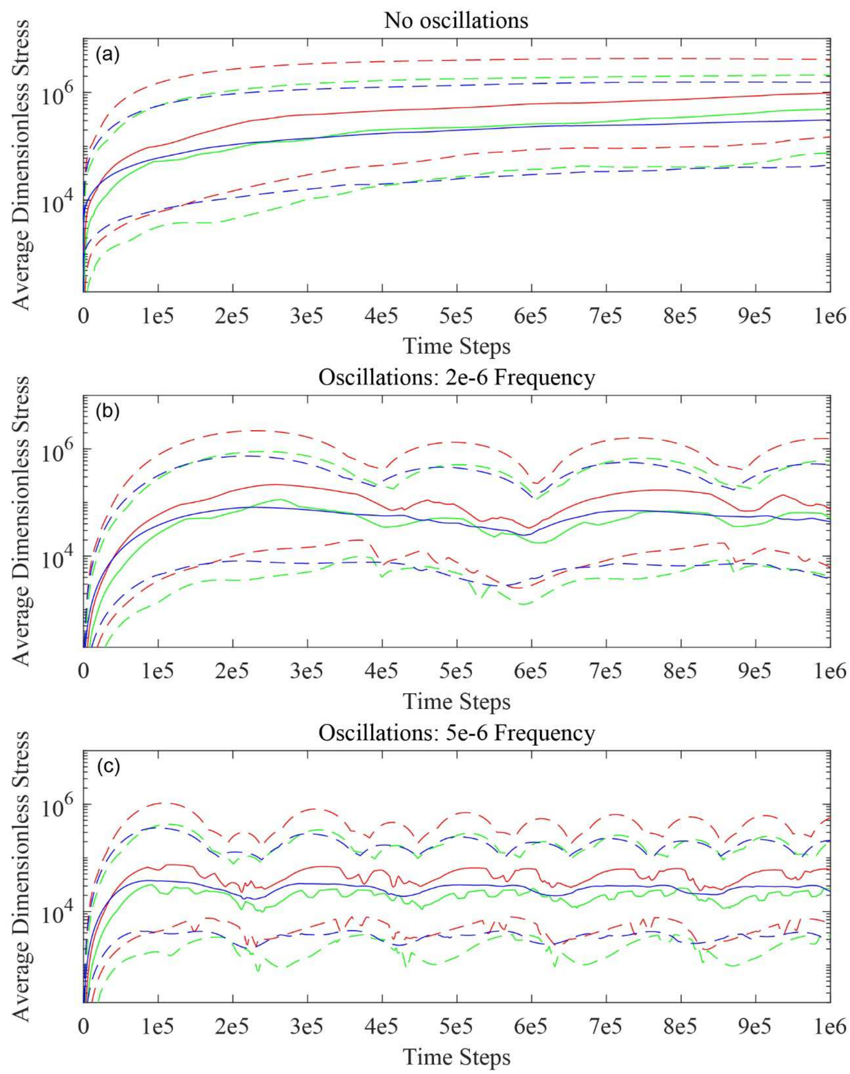

Fig. 11: The range of dimensionless force magnitudes experienced by each part of the cell (membrane/cortex (red), cytoskeleton/links (green), and processes (blue)) when using no oscillations a), oscillations with a lower (2e-6 cycles per timestep; b) and higher (5e-6 cycles per timestep; c) frequencies. The median, minimum, and maximum values across all cases for the indicated oscillation setting are plotted.

6. Summary and Discussion

We have developed a simple FSI model for fluid-osteocyte-process-interaction in a lacuno-canalicular system using the lattice Boltzmann immersed boundary framework in two dimensions. Although coarse-grained, the model consists of the major components of the fluid-osteocyte system including the osteocyte's membrane, cytoskeleton, cytosol, and processes in curved canaliculi and extracellular fluid. The model incorporates the mutual interactions among these components, including solid-solid and fluid-solid interactions in the case of static and cyclic loading. Such studies can help reveal what synergistic interplay may occur among these components and reveal new insights into osteocyte mechanotransduction. Here, we have considered such issues using many simulations with varied flow speeds and elastic stiffnesses. After analyzing, visualizing, and comparing our results, our major finding is that the part of osteocyte near the junctions between the cell body and the processes typically experience greater stress and strain, which indicate these regions are good candidates for being sites for osteocyte mechanosensors. Previous studies suggested that osteocyte processes are the primary sites for mechanosensation [13]. Our study, however, indicates that the stress and strain on the membrane could be greater than it is on the processes, indicating that the osteocyte body could also play an important role for mechanosensation.

Our results have indicated that, in such systems, motion of the osteocyte's main body may be dominated by a tendency for the cell to compress near inlet canaliculi, elongate towards outlet canaliculi, and be subjected to twisting or rotation by flow traveling from inlets to outlets. In our study, Fig. 3 shows how fluid can set up vortical like flow and encourage the cell to rotate. This tendency toward rotation, however, is significantly pronounced in our study due to the setup of the system that encourages counterclockwise flow in the non-oscillatory case. For randomly arranged canaliculi and in the presence of tethers that connect between focal adhesions on the cell's main body and the lacunar wall, we expect such an effect to be diminished if not entirely absent. Tethers can limit how far the cell can rotate and stop cells subject to non-oscillatory flow from rotating indefinitely. Still, in the presence of oscillatory flow, as in Fig. 4, smaller back-and-forth rotations as such cells may never hit the limits set by their tethers. In any case, such potential phenomenon will depend on multiple factors including osteocyte elasticity, frequency, tethering, and loading magnitude.

We also found that in terms of general motion, processes tend to stay centralized in the canaliculi as flow develops. They also seem to go faster down straight portions and slower down curved portions, probably related to release and storage of bending elastic energy and redirection of flow as it moves around the corner. The prevalence of this phenomenon, again, is subject to other factors not considered here including wall roughness and tethering of the process to the canalicular wall.

Investigation of stresses resulting in the system suggests that the membrane tends to be subjected to higher stresses than the other components. This was further supported by results from our factorial study that demonstrated similar high stresses for membranes across several simulations. At the same time, we made many simplifications to help our study focus primarily on the lowest order effects of geometry, interactions, and general trends as factors are varied. We assumed all components are infinitely thin, possess approximately the same elastic moduli, and can be used to approximate their cellular equivalents. As an example of the latter, our relatively simple elliptical membrane is meant to represent both the membrane and cortex. Obtaining more physiologically specific information for osteocytes such as the effective elastic moduli of the different components could alter these results to some degree that rely primarily on the geometry of our system and the interactions between components.

Investigation of the stresses and the internal stretches and bending in the solids also greatly emphasized the potential importance of process-osteocyte junctions. Our results suggested that near those junctions we can expect higher stresses as well as higher internal tension and twisting of solid components. These trends, again, are subject to quantitative adjustment if one considers making the system more physiologically realistic, for example, including thicker processes and membranes.

Our factorial study especially allowed us to see that oscillations, in general, can lead to lower average stresses. This is probably because it takes time for forces to develop since those forces grow as the object deforms more and more. During cyclic loading, structure deformations are regularly approximately reversed so that severe deformations and higher stresses are not reached. The stresses obtained, however, are still appreciable and repeatedly change directions. Given past evidence that low magnitude cyclic loading can, in fact, initiate significant responses [44], such forces may have implications for mechanotransduction.

The factorial study further found that increasing the Reynolds number or elastic moduli tends to increase non-dimensionalized stresses in the system. Perhaps more importantly, we saw that increasing the elastic moduli on one component affects the stresses experienced by all components due to coupled solid-solid and solid-fluid interactions. The components are interlinked and these results suggest that excluding such components from models can cause those studies to miss out on some insights.

The Reynolds number in our simulations varies from 0.0001 to 0.01. The stretching and bending elastic moduli for each cellular component (membrane, cytoskeleton, and processes) are $(\mathrm{K}_s, \mathrm{K}_\mathrm{b}) =$ (1.2 dyn/cm, 9e-10 dyn-cm) for more flexible scenarios; and $(K_s, K_b) =$ (12 dyn/cm, 9e-9 dyn-cm) for more rigid scenarios. The lower elastic moduli are chosen to match a previous study [45]. The values that we use are higher than the estimates for most cells [46-48]. For instance, red blood cells, which are relatively flexible compared to other cells, have estimated moduli of 0.012 dyn/cm and 1.2e-12 dyn-cm. Our choice to explore higher moduli ensures that cellular components stay reasonably far from the solid parts of the domain corresponding to the extracellular matrix (this can cause numerical issues). Despite this choice, we have still been able to identify general trends that may occur as those values are varied.

The top and bottom processes are tethered near the two north and south inlets/outlets and experience larger stresses there due to that tethering. Similarly, the right and left processes are assumed to be free. Neither of these situations represent physiological reality. While it is not immediately obvious how to best approximate what happens at inlets and outlets (osteocyte processes typically attach to each other in those regions), modeling the process ends more accurately may help produce more realistic and detailed results. This is especially at the inlet/outlet regions where we have currently avoided any in-depth analysis of the dynamics because of this issue.

Related are the boundary conditions at the ends of the canaliculi. They were designed assuming the north and south boundaries correspond to inlets and the east and west boundaries correspond to outlets. For oscillating flows, inlets and outlets switch. Though it is not immediately obvious that the boundary conditions should still work well, our results indicate that for the parameter ranges considered, no unrealistic behavior was encountered with many of our figures demonstrating approximate reversibility of cellular dynamics with no numerical instabilities arising preferentially in the oscillatory cases.

The process has been modeled using a one-dimensional fiber. While this is a good first approximation, including consideration of its girth in a model would help produce more physiologically realistic insights. Spreading out the stresses over a non-negligible outer surface could help lower the average stresses felt by the process. At the same time, the one-dimensional approximation overestimates the distance from the process to the canalicular wall so that including a finite width would lower that gap and raise the stress felt as fluid is forced through the narrower gap. Additional studies are needed to fully understand the implications of this approximation.

Given the characteristic length (lacuna width), speed (canalicular flow speed), mass density and dynamic viscosity of the interstitial fluid, one can calculate the Reynolds number Re and dimensionless stress via dimensional analysis. In particular, one obtains the following equation for converting dimensionless stress reported in the paper to dimensional stress:

$$\sigma_{phys} = \frac{\rho_{phys,char} u_{phys,char}^2}{\rho_{LB,char} u_{LB,char}^2} \sigma_{LB} = \rho_{phys,char}\, u_{phys,char}^2\, \sigma_{plot}$$
$$= \left(1000\,\frac{\mathrm{N}}{\mathrm{m}^2}\right) Re^2\, \sigma_{plot} \quad (18)$$

Here subscript "phys" means in physical units (SI units), "char" means characteristic quantity, "LB" means in LB units, "plot" means dimensionless quantities plotted in our figures. See Table 3 for some examples of dimensional stresses computed this way. For conversion to SI units, $\rho_{phys,char} = 1000$ kg/m^3, $u_{phys,char} = Re \cdot \nu_{phys,char}/L_{phys,char}$, $\nu_{phys,char} = 10^{-6}$ m^2/s, and $L_{phys,char} = 10^{-6}$ m (distance from lacunar membrane to wall) while $\rho_{LB} = 1$, $u_{LB,char} = Re \cdot \nu_{LB,char}/L_{LB,char}$, $\nu_{LB,char} = 1/6$, and $L_{LB,char} = 30$ for a 1024×1024 grid. When $Re = 0.001$, $\sigma_{phys} = 0.001\sigma_{plot}$, $u_{phys,in} = 1$ mm/s and $u_{LB,in} = 5.55 \times 10^{-6}$.

The interstitial fluid in the osteocyte-lacuna-canaliculi system could be non-Newtonian [49, 50]. We have assumed the fluid is Newtonian (water) in this work, as in almost all of the computational modeling involving osteocyte-fluid system in literature. References on oscillatory flows involving non-Newtonian fluids can be found in [51-54] and citations therein.

The lattice Boltzmann approach is a popular in computational fluid dynamics [27, 28, 30, 31, 55, 56]. However, the D2Q9 lattice Boltzmann model is very slow in reaching a steady state for low Reynolds numbers, as in our case. Other lattice Boltzmann models such as [57] or other approaches mentioned in [58] may be considered in the future for the osteocyte-fluid-lacuno-canalicular system.

While here we shared simulations that experienced no instabilities, there are parameter ranges where we encountered modeling challenges and numerical instabilities. If the Reynolds number is too high relative to the elastic moduli, this can lead to solid components approaching the lacuno-canalicular walls. In that case, the immersed boundary method can fail to model such interactions. If the Reynolds number is too low relative to the elastic moduli, this can be challenging for the lattice Boltzmann methods as it takes a very long time for the system to reach steady state or even to deform an appreciable amount. If both the Reynolds number and elastic moduli are high, this corresponds to faster flow with lower relative viscosity that can lead to oscillatory instabilities in the solid components. Such instabilities are solid-initiated, not fluid-initiated, as they are effectively composed of relatively stiff springs compared to the surrounding weakly dampening fluid viscosity. These limitations make the method only conditionally stable. Our experience with the method further shows that some of the associated instabilities may not occur until after many timesteps have been taken. Improving the LB-IB method, especially its numerical stability (perhaps starting with ideas introduced in [59]), is of significant interest in our future work.

ACKNOWLEDGEMENTS

L Zhu and J Barber thank the support of the US NSF under the research grant DMS-1951531 and IUPUI SoS Near-Miss grant. Isaac Manring was supported by NSF research grant DMS-1951531 and Sophie Boileau was supported by the NSF REU grant DMS-1852146. L Zhu and J Barber thank Drs. S Na and H Yokota for discussion.

Author Declarations

The authors have no conflicts to disclose.

Data Availability Statement

The data that support the findings of this study are available from the corresponding author upon reasonable request.

Appendix A

Differentiating Eq. 15 (principle of virtual work; $-\frac{\partial \mathcal{E}_b}{\partial \mathbf{X}_l}$) and using Eq. 16, which provides a discrete approximation to the curvature, yields that the force on the fiber (with original equidistant spacing between points of $\Delta\alpha$) at location $\mathbf{X}_l = \langle X_l, Y_l \rangle$ is given by:

$$\mathbf{F}_{b,l} =$$

$$\begin{aligned}
&-k_b \Delta\alpha \Bigg((\kappa_{l-1} - \kappa_{l-1,0}) \left(\frac{8}{\|\mathbf{X}_l - \mathbf{X}_{l-2}\|^3} \begin{bmatrix} Y_{l-2} - Y_{l-1} \\ X_{l-1} - X_{l-2} \end{bmatrix} - \frac{24(\mathbf{X}_{l-1} - \mathbf{X}_{l-2}) \times (\mathbf{X}_l - \mathbf{X}_{l-1}) \cdot \hat{k}}{\|\mathbf{X}_l - \mathbf{X}_{l-2}\|^5} \begin{bmatrix} X_l - X_{l-2} \\ Y_l - Y_{l-2} \end{bmatrix} \right) \\
&\qquad + (\kappa_l - \kappa_{l,0}) \left(\frac{8}{\|\mathbf{X}_{l+1} - \mathbf{X}_{l-1}\|^3} \begin{bmatrix} Y_{l+1} - Y_{l-1} \\ X_{l-1} - X_{l+1} \end{bmatrix} \right) + \\
&\quad (\kappa_{l+1} - \kappa_{l+1,0}) \left(\frac{8}{\|\mathbf{X}_{l+2} - \mathbf{X}_l\|^3} \begin{bmatrix} Y_{l+1} - Y_{l+2} \\ X_{l+2} - X_{l+1} \end{bmatrix} + \frac{24(\mathbf{X}_{l+1} - \mathbf{X}_l) \times (\mathbf{X}_{l+2} - \mathbf{X}_{l+1}) \cdot \hat{k}}{\|\mathbf{X}_{l+2} - \mathbf{X}_l\|^5} \begin{bmatrix} X_{l+2} - X_l \\ Y_{l+2} - Y_l \end{bmatrix} \right) \Bigg)
\end{aligned}$$

This formula yields a five-point stencil along the fiber. For the ends, the discrete energy for a fiber with nf points, which assumes zero curvature at the ends, is given by:

$$\mathbf{F}_{b,l} = -\frac{\partial E_b}{\partial \mathbf{X}_l} = -k_b \Delta\alpha \sum_{i=2}^{nf-1} (\kappa_i - \kappa_{i,0}) \frac{\partial \kappa_i}{\partial \mathbf{X}_l}$$

$$= -k_b \Delta\alpha \left((\kappa_{l-1} - \kappa_{l-1,0}) \frac{\partial \kappa_{l-1}}{\partial \mathbf{X}_l} + (\kappa_l - \kappa_{l,0}) \frac{\partial \kappa_l}{\partial \mathbf{X}_l} + (\kappa_{l+1} - \kappa_{l+1,0}) \frac{\partial \kappa_{l+1}}{\partial \mathbf{X}_l} \right)$$

If $l = 2$ or $nf - 1$, only two terms survive the differentiation process. For $l = 2$:

$$\mathbf{F}_{b,2} = -k_b \Delta\alpha \left((\kappa_2 - \kappa_{2,0}) \frac{\partial \kappa_2}{\partial \mathbf{X}_2} + (\kappa_3 - \kappa_{3,0}) \frac{\partial \kappa_3}{\partial \mathbf{X}_2} \right)$$

For $l = nf - 1$:

$$\mathbf{F}_{b,nf-1} = -k_b \Delta\alpha \left((\kappa_{nf-2} - \kappa_{nf-2,0}) \frac{\partial \kappa_{nf-2}}{\partial \mathbf{X}_{nf-1}} + (\kappa_{nf-1} - \kappa_{nf-1,0}) \frac{\partial \kappa_{nf-1}}{\partial \mathbf{X}_{nf-1}} \right)$$

Similarly for $l = 1$:

$$\mathbf{F}_{b,1} = -k_b \Delta\alpha \left((\kappa_2 - \kappa_{2,0}) \frac{\partial \kappa_2}{\partial \mathbf{X}_1} \right).$$

For $l = nf$:

$$\mathbf{F}_{b,nf} = -k_b \Delta\alpha \left((\kappa_{nf-1} - \kappa_{nf-1,0}) \frac{\partial \kappa_{nf-1}}{\partial \mathbf{X}_{nf}} \right)$$

To avoid recalculating quantities, we note that the general formula

$$\mathbf{F}_{b,l} = -k_b \Delta\alpha \left((\kappa_{l-1} - \kappa_{l-1,0}) \frac{\partial \kappa_{l-1}}{\partial \mathbf{X}_l} + (\kappa_l - \kappa_{l,0}) \frac{\partial \kappa_l}{\partial \mathbf{X}_l} + (\kappa_{l+1} - \kappa_{l+1,0}) \frac{\partial \kappa_{l+1}}{\partial \mathbf{X}_l} \right)$$

can be rewritten by defining

$$\mathbf{a}_l = \begin{cases} (\kappa_{l-1} - \kappa_{l-1,0}) \dfrac{\partial \kappa_{l-1}}{\partial \mathbf{X}_l} & 2 < l \\ 0 & otherwise \end{cases}$$

$$\mathbf{b}_l = \begin{cases} (\kappa_l - \kappa_{l,0}) \dfrac{\partial \kappa_l}{\partial \mathbf{X}_l} & 1 < l < nf \\ 0 & otherwise \end{cases}$$

$$\mathbf{c}_l = \begin{cases} (\kappa_{l+1} - \kappa_{l+1,0}) \dfrac{\partial \kappa_{l+1}}{\partial \mathbf{X}_l} & l < nf - 1 \\ 0 & otherwise \end{cases}$$

Then we can first calculate the discrete approximants to the curvatures:

$$\kappa_l = 8 \frac{(\mathbf{X}_l - \mathbf{X}_{l-1}) \times (\mathbf{X}_{l+1} - \mathbf{X}_l)}{\|\mathbf{X}_{l+1} - \mathbf{X}_{l-1}\|^3} \cdot \hat{\mathbf{z}}.$$

Then we define and find:

$$d_l = \kappa_l - \kappa_{l,0}$$

$$\boldsymbol{\alpha}_l = \frac{\partial \kappa_{l-1}}{\partial \mathbf{X}_l} = \frac{8}{\|\mathbf{X}_l - \mathbf{X}_{i-2}\|^3} \begin{bmatrix} Y_{l-2} - Y_{l-1} \\ X_{l-1} - X_{l-2} \end{bmatrix} - \frac{24 (\mathbf{X}_{l-1} - \mathbf{X}_{l-2}) \times (\mathbf{X}_l - \mathbf{X}_{l-1}) \cdot \hat{\mathbf{z}}}{\|\mathbf{X}_l - \mathbf{X}_{l-2}\|^5} \begin{bmatrix} X_l - X_{l-2} \\ Y_l - Y_{l-2} \end{bmatrix}$$

$$\boldsymbol{\beta}_l = \frac{\partial \kappa_l}{\partial \mathbf{X}_l} = \frac{8}{\|\mathbf{X}_{l+1} - \mathbf{X}_{l-1}\|^3} \begin{bmatrix} Y_{l+1} - Y_{l-1} \\ X_{l-1} - X_{l+1} \end{bmatrix}$$

$$\boldsymbol{\gamma}_l = \frac{\partial \kappa_{l+1}}{\partial \mathbf{X}_l} = \frac{8}{\|\mathbf{X}_{l+2} - \mathbf{X}_l\|^3} \begin{bmatrix} Y_{l+1} - Y_{l+2} \\ X_{l+2} - X_{l+1} \end{bmatrix} + \frac{24 (\mathbf{X}_{l+1} - \mathbf{X}_l) \times (\mathbf{X}_{l+2} - \mathbf{X}_{l+1}) \cdot \hat{\mathbf{z}}}{\|\mathbf{X}_{l+2} - \mathbf{X}_l\|^5} \begin{bmatrix} X_{l+2} - X_l \\ Y_{l+2} - Y_l \end{bmatrix}$$

Then we can recover the force using:

$$\mathbf{a}_l = \begin{cases} d_{l-1} \boldsymbol{\alpha}_l & 2 < l \\ 0 & otherwise \end{cases}$$

$$\mathbf{b}_l = \begin{cases} d_l \boldsymbol{\beta}_l & 1 < l < nf \\ 0 & otherwise \end{cases}$$

$$\mathbf{c}_l = \begin{cases} d_{l+1} \boldsymbol{\gamma}_l & l < nf - 1 \\ 0 & otherwise \end{cases}$$

$$\mathbf{F}_{b,l} = -k_b \Delta\alpha (\mathbf{a}_l + \mathbf{b}_l + \mathbf{c}_l)$$

This yields a discretized estimate for the bending force used in our model.

Appendix B

For high moduli and long run times, the force estimates obtained using the principal of virtual work applied to the solid components were found to oscillate in magnitude and direction when moving along the solid components (membrane and processes). Because of this tendency, we instead estimated the forces on the solid components by using the fluid stress tensor that is defined on the fluid mesh and radial basis functions to extrapolate information from that fluid mesh to the solid mesh. With the individual stress tensor components (and pressure = density/3) extrapolated to the solid component mesh, the stress vector $\mathbf{\Sigma} = \boldsymbol{\sigma} \cdot \hat{\mathbf{n}}$ and other quantities were easily obtained.

While the initial fluid mesh is rectilinear, bilinear (or similar) interpolation techniques are not appropriate because stresses can experience discontinuities across a membrane (see, for example, the law of Laplace). This is further complicated by the immersed boundary method that tends to smooth out such discontinuities which can give the false impression that the stress jump across the membrane is much smaller than it actually is. To avoid both of these issues, only fluid points that were more than 2 fluid mesh units away from the solid components were used in the extrapolation process. Using only this subset of points produced a scattered non-rectilinear set of points, which radial basis functions readily handle.

Using a similar approach to Renka's ([34]; a quadratic Shepard interpolant), we employed the following algorithm to estimate functional values (stress tensor components and pressure/density) at target locations (solid nodes) using functional values at source locations (scattered fluid nodes). We also used the algorithm to calculate fluid velocity derivatives, which we used to verify that the LBM code calculated the stress tensor at the fluid nodes correctly.

1. For each of the N source locations, $\mathbf{x}_{si} = \langle x_{si}, y_{si} \rangle$, find the nearest $n = 20$ source locations (including the original point) and find a quadratic function of the form $q_{si}(x, y) = f(x_{si}, y_{si}) + c_{10i}(x - x_{si}) + c_{01i}(y - y_{si}) + c_{20i}(x - x_{si})^2 + c_{11i}(x - x_{si})(y - y_{si}) + c_{02i}(y - y_{si})^2$ that best fits the data $f(x_{si}, y_{si})$ through those closest points, in a least squares sense. Note that forcing q_{si} to pass through $f(x_{si}, y_{si})$ ensures the local interpolant passes exactly through the value of f at that location.
2. For each of the M target locations, $\mathbf{x}_{tj} = \langle x_{tj}, y_{tj} \rangle$:
   a. Use the quadratic equations from the nearest $n = 20$ source points, indexed by $i_{1j}, i_{2j}, \dots, i_{nj}$, to get multiple estimates for the function value at the target location: $Q_{i_{kj}j} = q_{si_{kj}}(x_{tj}, y_{tj})$. This quantity is only found for the 20 values of i that correspond to the closest source points.
   b. Use radial basis functions to combine the estimates: $\tilde{f}(x_{tj}, y_{tj}) = \frac{\sum_{k=1}^{n} Q_{i_{kj}j}\phi(|\mathbf{x}_j - \mathbf{x}_{i_{kj}}|)}{\sum_{k=1}^{n} \phi(|\mathbf{x}_j - \mathbf{x}_{i_{kj}}|)}$ where $\phi(r) = r^{-2}$.
3. To obtain derivatives at each target location, differentiate the quadratic functions with respect to x and y and use radial basis functions to combine: $\tilde{f}_x(x_{tj}, y_{tj}) = \frac{\sum_{k=1}^{n} q_{si_{kj},x}(x_{tj}, y_{tj})\phi(|\mathbf{x}_j - \mathbf{x}_{i_{kj}}|)}{\sum_{i=1}^{n} \phi(|\mathbf{x}_j - \mathbf{x}_i|)}$; $\tilde{f}_y(x_{tj}, y_{tj}) = \frac{\sum_{i=1}^{N} q_{si,y}(x_{tj}, y_{tj})\phi(|\mathbf{x}_j - \mathbf{x}_i|)}{\sum_{i=1}^{N} \phi(|\mathbf{x}_j - \mathbf{x}_i|)}$.

We performed convergence tests (Fig. 12) to ensure that this program works correctly by comparing estimates for $f(x, y) = \exp{(x + 2y)}$ using a 10×10 square grid of source points of various sizes to estimate values and derivatives for 100 randomly chosen (uniform distribution) target points within the span of the grid. The convergence tests clearly show $O(h^3)$ error for values and $O(h^2)$ error for derivatives, as expected for the quadratic-based interpolants.

Before trying radial basis functions, we employed a simpler strategy. For each target location, we found the $n = 20$ nearest source locations, fit a quadratic, and then used the quadratic to estimate functional values and derivatives at the target location. While this took less time, results from the radial basis function approach were significantly smoother. For that reason, we presented the results obtained from the radial basis function approach.

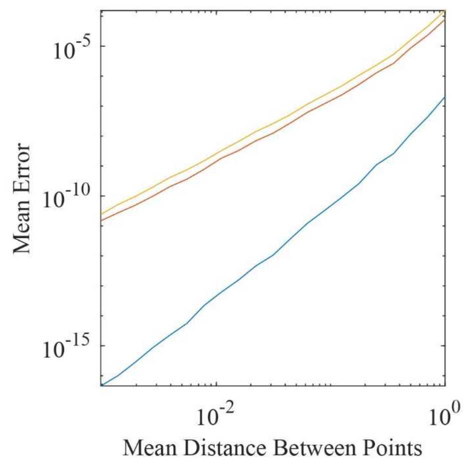

Fig. 12: Convergence results for interpolation using our radial basis function approach. Slopes for this standard convergence plot are 2 and 3 corresponding to $O(h^2)$ and $O(h^3)$ convergence.

To further show the appropriateness of our strategy, we include a picture (Fig. 13) of the LBM-estimated fluid density (blue surface) and the radial basis estimated fluid density at the boundary. Note that the discontinuity between internal vs. external density is smoothed out by the immersed boundary method as one crosses the membrane. The radial basis function, however, relying on points far away from the boundary relatively smoothly and accurately extrapolates the density to the membrane boundary while ignoring immersed boundary smoothing effects.

Calculating fluid stresses is accomplished by starting with estimates for fluid stresses everywhere in the fluid (Eq. 14). For a given component (membrane or process), all points within 2 units of the component are found and ignored. In addition, to focus on "external" flow, all points on the "internal" side of the components are likewise found and ignored. For the membrane, all points on the inside of the membrane are ignored. For the process, to find σ_+, all points on the negative side are found and ignored while for σ_-, all points on the positive side are found and ignored. This leaves only points and corresponding fluid stress tensor component (and pressure) values in the "external" fluid. These points and values are used with the radial basis functions to extrapolate the fluid values onto the solid grid. Further calculations are performed as described in subsection 5.2.

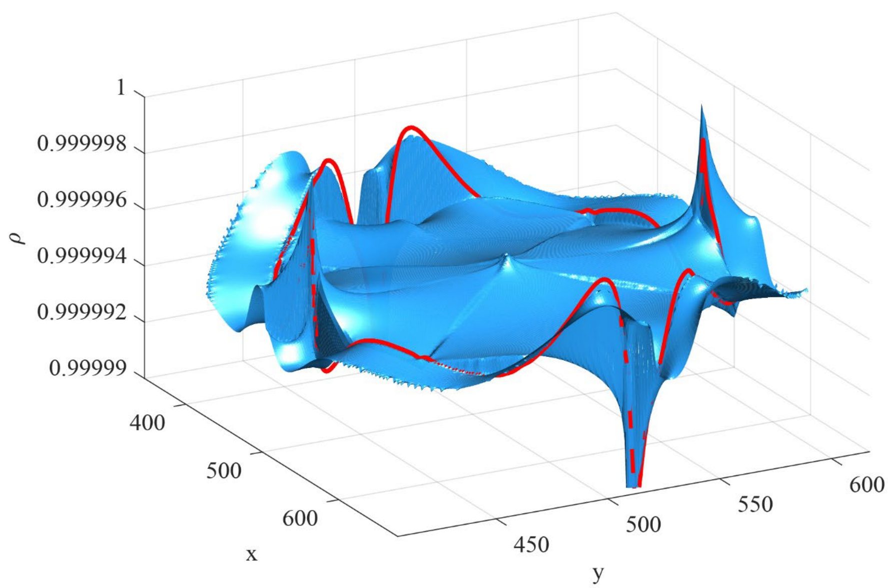

Fig. 13: Results of radial basis interpolation for finding ρ, the density of the fluid in the osteocyte region. The functions extrapolate the data from the external fluid to obtain a reasonable estimate for the values of the fluid density on the outside of the membrane.

Appendix C

An ideal convergence study would compare approximate solutions to an exact solution. As we have no exact analytical solution, we instead compared the relative differences between solutions on successively refined meshes using n^2, $(2n)^2$, $(4n)^2$, etc. points. If we expect the error $\mathbf{e}(n) = \mathbf{s}_a(n) - \mathbf{s}_e(n) = \mathcal{O}(1/n^p)$ ($\mathbf{s}_a(n)$ and $\mathbf{s}_e(n)$ are approximate and exact solutions, respectively), as the refinement level increases, we expect $\mathbf{e}(n) \approx \mathbf{C}/n^p$. This can be used to show

$$p \approx \log_2 \frac{\|\mathbf{e}(n) - \mathbf{e}(2n)\|}{\|\mathbf{e}(2n) - \mathbf{e}(4n)\|} \approx \log_2 \frac{\|\mathbf{s}_a(n) - \mathbf{s}_a(2n)\|}{\|\mathbf{s}_a(2n) - \mathbf{s}_a(4n)\|}.$$

For the Lattice Boltzmann method, $p = 2$ [30] while for the immersed boundary method, when it involves an infinitesimally thin/sharp interface, as seen here, $p = 1$ [38]. Further, successive differences in approximate solutions are related by $\|\mathbf{s}_a(2n) - \mathbf{s}_a(4n)\| \approx \|\mathbf{s}_a(n) - \mathbf{s}_a(2n)\|/2^p$ so that such differences are halved ($p = 1$) or quartered ($p = 2$) as the grids are further refined.

To quantify convergence, we compared fluid velocities and pressure and solid positions for successively refined grids. For fluid velocities, bilinear interpolation is used to find fluid quantities on the coarser grid (e.g. $\mathbf{u}(2n) \to \mathbf{u}_{coarse}(2n)$) and then the velocities and pressures from the coarser and finer grids were compared at those locations. Fair comparison required first nondimensionalizing quantities. We considered the relative l_1 norm for the horizontal velocity u (similarly for v and p):

$$\|\mathbf{s}_a(n) - \mathbf{s}_a(2n)\| = \|\mathbf{e}(n) - \mathbf{e}(2n)\| \approx \frac{\sum_{ij}\left|\tilde{u}_{ij,coarse}(2n) - \tilde{u}_{ij}(n)\right|/n}{\sum_{ij}\left|\tilde{u}_{ij}(n)\right|/n}.$$

The sums are over all fluid nodes. This gives the estimated average fractional difference between successive solutions with smaller values indicating convergence.

For displacements, comparisons were enabled by considering the nondimensionalized positions of the solid nodes, indexed by i: $\tilde{\mathbf{x}}_i(n) = (\mathbf{x}_i(n) - \mathbf{x}_0)/n$ where $\mathbf{x}_0 = \langle n-1, n-1\rangle/2$. The placement of the solid fibers has been handled so that $\left(\tilde{x}_i(n) - \tilde{x}_{2i-1}(2n)\right) = \mathcal{O}(\Delta\alpha^2)$ at the start of each simulation. Hence, we compare those locations at later times:

$$\|\mathbf{s}_a(n) - \mathbf{s}_a(2n)\| \approx \frac{\sum_i |\tilde{x}_{2i-1}(2n) - \tilde{x}_i(n)|}{\sum_i 1}$$

The sums are over all solid nodes for the coarser mesh or over every other solid node for the finer mesh. This gives the average amount of deviation of the coarse solid fiber locations from the finer fiber locations or the average distance between the coarse solid and fine solid solution. Results can be found in Table 1 and are discussed in text.

REFERENCES

1. Qin, L., et al., *Molecular mechanosensors in osteocytes.* Bone research, 2020. **8**(1): p. 1-24.
2. Robling, A.G. and L.F. Bonewald, *The osteocyte: new insights.* Annual review of physiology, 2020. **82**: p. 485-506.
3. Weinbaum, S., S. Cowin, and Y. Zeng, *A model for the excitation of osteocytes by mechanical loading-induced bone fluid shear stresses.* Journal of biomechanics, 1994. **27**(3): p. 339-360.
4. Klein-Nulend, J., et al., *Sensitivity of osteocytes to biomechanical stress in vitro.* The FASEB Journal, 1995. **9**(5): p. 441-445.
5. You, L., et al., *A model for strain amplification in the actin cytoskeleton of osteocytes due to fluid drag on pericellular matrix.* Journal of biomechanics, 2001. **34**(11): p. 1375-1386.
6. Han, Y., et al., *Mechanotransduction and strain amplification in osteocyte cell processes.* Proceedings of the National Academy of Sciences of the United States of America, 2004. **101**(47): p. 16689-16694.
7. Wang, Y., et al., *A model for the role of integrins in flow induced mechanotransduction in osteocytes.* Proceedings of the National Academy of Sciences, 2007. **104**(40): p. 15941-15946.
8. Anderson, E.J. and M.L.K. Tate, *Idealization of pericellular fluid space geometry and dimension results in a profound underprediction of nano-microscale stresses imparted by fluid drag on osteocytes.* Journal of biomechanics, 2008. **41**(8): p. 1736-1746.
9. Kamioka, H., et al., *Microscale fluid flow analysis in a human osteocyte canaliculus using a realistic high-resolution image-based three-dimensional model.* Integrative Biology, 2012. **4**(10): p. 1198-1206.
10. Verbruggen, S.W., T.J. Vaughan, and L.M. McNamara, *Strain amplification in bone mechanobiology: a computational investigation of the in vivo mechanics of osteocytes.* Journal of the Royal Society Interface, 2012. **9**(75): p. 2735-2744.
11. Wang, L., J. Dong, and C.J. Xian, *Strain Amplification Analysis of an Osteocyte under Static and Cyclic Loading: A Finite Element Study.* BioMed research international, 2015. **2015**(Article ID 376474).
12. Schurman, C.A., S.W. Verbruggen, and T. Alliston, *Disrupted osteocyte connectivity and pericellular fluid flow in bone with aging and defective TGF-β signaling.* Proceedings of the National Academy of Sciences, 2021. **118**(25).

13. Verbruggen, S.W., T.J. Vaughan, and L.M. McNamara, *Fluid flow in the osteocyte mechanical environment: a fluid-structure interaction approach.* Biomechanics and modeling in mechanobiology, 2014. **13**(1): p. 85-97.
14. Vaughan, T., et al., *Bone cell mechanosensation of fluid flow stimulation: a fluid-structure interaction model characterising the role integrin attachments and primary cilia.* Biomechanics and modeling in mechanobiology, 2014. **14**(4): p. 703-718.
15. Verbruggen, S.W., T.J. Vaughan, and L.M. McNamara, *Mechanisms of osteocyte stimulation in osteoporosis.* Journal of the mechanical behavior of biomedical materials, 2016. **62**: p. 158-168.
16. Joukar, A., H. Niroomand-Oscuii, and F. Ghalichi, *Numerical simulation of osteocyte cell in response to directional mechanical loadings and mechanotransduction analysis: considering lacunar-canalicular interstitial fluid flow.* Computer Methods and Programs in Biomedicine, 2016.
17. Kameo, Y., M. Ozasa, and T. Adachi, *Computational framework for analyzing flow-induced strain on osteocyte as modulated by microenvironment.* Journal of the Mechanical Behavior of Biomedical Materials, 2022. **126**: p. 105027.
18. Ganesh, T., et al., *Multiscale finite element modeling of mechanical strains and fluid flow in osteocyte lacunocanalicular system.* Bone, 2020. **137**: p. 115328.
19. Zhu, L., et al., *An immersed boundary method based on the lattice Boltzmann approach in three dimensions, with application.* Computers & Mathematics with Applications, 2011. **61**(12): p. 3506-3518.
20. Zhu, L., et al., *A deformable plate interacting with a non-Newtonian fluid in three dimensions.* Physics of Fluids, 2017. **29**(8): p. 083101.
21. Zhu, L., *An IB Method for Non-Newtonian-Fluid Flexible-Structure Interactions in Three-Dimensions.* Computer Modeling in Engineering & Sciences, 2019. **119**(1): p. 125-143.
22. You, L.-D., et al., *Ultrastructure of the osteocyte process and its pericellular matrix.* The Anatomical Record Part A: Discoveries in Molecular, Cellular, and Evolutionary Biology, 2004. **278**(2): p. 505-513.
23. Sugawara, Y., et al., *Three-dimensional reconstruction of chick calvarial osteocytes and their cell processes using confocal microscopy.* Bone, 2005. **36**(5): p. 877-83.
24. Hannah, K., et al., *Bimodal distribution of osteocyte lacunar size in the human femoral cortex as revealed by micro-CT.* Bone, 2010. **47**(5): p. 866-871.
25. Anderson, E.J., et al., *Nano-microscale models of periosteocytic flow show differences in stresses imparted to cell body and processes.* Annals of biomedical engineering, 2005. **33**(1): p. 52-62.
26. Peskin, C.S., *The immersed boundary method.* Acta Numerica, 2002. **11**: p. 479-517.
27. Succi, S. and S. Succi, *The lattice Boltzmann equation: for complex states of flowing matter*. 2018: Oxford University Press.
28. Huang, H., M. Sukop, and X. Lu, *Multiphase lattice Boltzmann methods: Theory and application*. 2015: John Wiley & Sons.
29. Guo, Z. and C. Shu, *Lattice Boltzmann method and its applications in engineering*. Vol. 3. 2013: World Scientific.
30. Krüger, T., et al., *The lattice Boltzmann method.* Springer International Publishing, 2017. **10**(978-3): p. 4-15.
31. Wolf-Gladrow, D.A., *Lattice-gas cellular automata and lattice Boltzmann models: An Introduction*. 2000: Springer.
32. Zhu, L., et al., *Modeling and simulation of interstitial fluid flow around an osteocyte in a lacuno-canalicular network.* Physics of Fluids, 2022. **34**(4): p. 041906.

33. Bao, Y.B. and J. Meskas, *Lattice Boltzmann method for fluid simulations.* Department of Mathematics, Courant Institute of Mathematical Sciences, New York University, 2011. **44**.
34. Renka, R.J., *Qshep2d - Quadratic Shepard Method for Bivariate Interpolation of Scattered Data.* Acm Transactions on Mathematical Software, 1988. **14**(2): p. 149-150.
35. Chen, S. and G.D. Doolen, *Lattice Boltzmann method for fluid flows.* Annual Review of Fluid Mechanics, 1998. **30**: p. 329-364.
36. Bai, Z. and L. Zhu, *3D simulation of a viscous flow past a compliant model of arteriovenous-graft annastomosis.* Computers & Fluids, 2019. **181**: p. 403-415.
37. Bai, Z. and L. Zhu, *Simulation of Blood Flow past a Distal Arteriovenous-Graft Anastomosis at Low Reynolds Numbers.* Physics of Fluids, Accepted, August 2019., 2019.
38. Griffith, B.E. and C.S. Peskin, *On the order of accuracy of the immersed boundary method: Higher order convergence rates for sufficiently smooth problems.* Journal of Computational Physics, 2005. **208**(1): p. 75-105.
39. !!! INVALID CITATION !!! .
40. Cardoso, L., et al., *Advances in assessment of bone porosity, permeability and interstitial fluid flow.* Journal of biomechanics, 2013. **46**(2): p. 253-265.
41. Florencio-Silva, R., et al., *Biology of bone tissue: structure, function, and factors that influence bone cells.* BioMed research international, 2015. **2015**.
42. Kwon, R.Y. and J.A. Frangos, *Quantification of lacunar–canalicular interstitial fluid flow through computational modeling of fluorescence recovery after photobleaching.* Cellular and molecular bioengineering, 2010. **3**(3): p. 296-306.
43. Buenzli, P.R. and N.A. Sims, *Quantifying the osteocyte network in the human skeleton.* Bone, 2015. **75**: p. 144-150.
44. Lau, E., et al., *Effect of low-magnitude, high-frequency vibration on osteocytes in the regulation of osteoclasts.* Bone, 2010. **46**(6): p. 1508-1515.
45. Barber, J. and L. Zhu. *Mathematical and mechanical models of cell motion*.
46. Secomb, T.W., B. Styp-Rekowska, and A.R. Pries, *Two-dimensional simulation of red blood cell deformation and lateral migration in microvessels.* Annals of Biomedical Engineering, 2007. **35**(5): p. 755-765.
47. Wu, X.T., et al., *The potential role of spectrin network in the mechanotransduction of MLO-Y4 osteocytes.* Sci Rep, 2017. **7**: p. 40940.
48. Strychalski, W., et al., *A poroelastic immersed boundary method with applications to cell biology.* Journal of Computational Physics, 2015. **282**: p. 77-97.
49. Lemaire, T., S. Naïli, and A. Rémond, *Study of the influence of fibrous pericellular matrix in the cortical interstitial fluid movement with hydroelectrochemical effects.* Journal of biomechanical engineering, 2008. **130**(1).
50. Kumar, R., et al., *Electromagnetic Field Induced Alterations in Fluid Flow through Lacuno-Canalicular System of Bone.* International Journal of Mechanical Sciences, 2021: p. 107036.
51. Gilbert, P.H. and A.J. Giacomin, *Molecular origins of higher harmonics in large-amplitude oscillatory shear flow: Shear stress response.* Physics of Fluids, 2016. **28**(10): p. 103101.
52. Saengow, C., A.J. Giacomin, and C. Kolitawong, *Exact analytical solution for large-amplitude oscillatory shear flow from Oldroyd 8-constant framework: Shear stress.* Physics of Fluids, 2017. **29**(4): p. 043101.
53. Jbara, L.M., A.J. Giacomin, and C. Saengow, *Pattern method for higher harmonics of first normal stress difference from molecular orientation in oscillatory shear flow.* Physics of Fluids, 2020. **32**(3): p. 031704.
54. Giacomin, A., L. Jbara, and C. Saengow, *Pattern method for higher harmonics from macromolecular orientation in oscillatory shear flow.* Physics of Fluids, 2020. **32**(1): p. 011703.

55. Petersen, K. and J. Brinkerhoff, *On the lattice Boltzmann method and its application to turbulent, multiphase flows of various fluids including cryogens: A review.* Physics of Fluids, 2021. **33**(4): p. 041302.
56. Li, S., et al., *Prediction of three-phase relative permeabilities of Berea sandstone using lattice Boltzmann method.* Physics of Fluids, 2021. **33**(6): p. 063302.
57. Khirevich, S. and T.W. Patzek, *Behavior of numerical error in pore-scale lattice Boltzmann simulations with simple bounce-back rule: Analysis and highly accurate extrapolation.* Physics of Fluids, 2018. **30**(9): p. 093604.
58. Phan, A., D. Fan, and A. Striolo, *Fluid transport through heterogeneous pore matrices: Multiscale simulation approaches.* Physics of Fluids, 2020. **32**(10): p. 101301.
59. Chen, H., P. Yu, and C. Shu, *A unified immersed boundary-lattice Boltzmann flux solver (UIB-LBFS) for simulation of flows past porous bodies.* Physics of Fluids, 2021. **33**(8).